USGS Award Numbers: G14AP00118 & G14AP00119

Probabilistic Liquefaction Potential and Lateral Spread Hazard Maps for Utah County, Utah: Collaborative Research with Brigham Young University and Oregon State University

Prepared For:

United States Geological Survey

Utah Department of Transportation

Central Utah Water Conservancy District

Submitted and Authored By:

Daniel T. Gillins, Ph.D., P.L.S.
Assistant Professor
101 Kearney Hall
School of Civil and Construction Engineering
Oregon State University
Corvallis, OR 97331
541-737-4865 (voice)
541-737-3052 (fax)
Email: dan.gillins@oregonstate.edu

Kevin Franke, Ph.D., P.E.
Assistant Professor
368P Clyde Building
Civil and Environmental Engineering
Brigham Young University
Provo, UT 84602
801-422-1349 (voice)
801-422-0159 (fax)
Email: kfranke@et.byu.edu

Term of Award:
08/01/2014 – 01/31/2016

Abstract

Utah's intermountain valleys along the western edge of the Wasatch Front contain widespread deposits of loose, saturated, cohesionless soils that are susceptible to liquefaction during major, nearby earthquakes. Liquefaction can induce ground deformations that can be very damaging to buildings, roadways, bridges, pipelines, buried structures, etc. The most pervasive type of liquefaction-induced ground deformation is lateral spreading, where blocks of mostly intact soil above a layer of liquefied soil may displace down gentle slopes up to tens of feet, thereby compressing or tearing apart foundations, crippling utility lines, damaging roadways, etc. To address this hazard, probabilistic-based hazard assessment is an important component in quantifying the risk and reducing potential losses from earthquakes. The development of probabilistic national seismic hazard maps and the adoption of these maps by various building codes and government agencies allow for the development of complementary liquefaction triggering and ground deformation hazard maps. Liquefaction and ground deformation hazard maps assist hazard planners, emergency responders, risk analysts, and public/private decision makers in the preliminary and/or regional assessment of liquefaction hazard. In addition, they help prioritize and complement site-specific liquefaction and lateral spread hazard evaluation procedures. This report presents the development of a new, fully-probabilistic procedure for mapping liquefaction triggering and lateral spread displacements at multiple return periods. It incorporates performance-based models for liquefaction triggering (Kramer and Mayfield 2007) and lateral spread displacement (Franke and Kramer 2013). The procedure is applied to develop liquefaction triggering and lateral spread displacement hazard maps for Utah County, Utah at return periods of 475, 1033, and 2475 years.

Table of Contents

1. Introduction ... 1
1.1 Problem Statement ... 1
1.2 Objectives ... 2
1.3 Research Tasks ... 3
1.4 Report Organization ... 4
2. Background ... 5
2.1 Previous Mapping Effort in Utah County ... 5
2.2 Background on Liquefaction Hazard Evaluation ... 7
2.2.1 Susceptibility ... 7
2.2.2 Triggering ... 10
2.2.3 Consequence - Lateral Spreading ... 17
3. Data Compilation ... 20
3.1 Geological Mapping ... 20
3.2 Geotechnical Database ... 21
3.3 Topographical Data ... 23
4. Liquefaction Triggering Mapping ... 26
4.1 Analysis of SPT Boreholes in the Utah County Geotechnical Database ... 26
4.2 Performance-Based Liquefaction Triggering Model ... 33
4.3 Seismic Hazard Analysis ... 34
4.4 Probabilistic Liquefaction Triggering Mapping Procedure ... 40
4.4.1. Step 1: Extract Raster Data at a Map Pixel ... 41
4.4.2. Step 2: Begin Monte Carlo Simulations, Select an SPT log ... 42
4.4.3. Step 3: Input a_{max} and M ... 43
4.4.4. Step 4: Solve for CSR, CRR and FS_L ... 45
4.4.5. Step 5: Repeat Steps 2 – 4 for Required Number of Simulations ... 46
4.4.6. Step 6: Develop FS_L Hazard Curve ... 46
4.4.7. Step 7: Repeat Previous Steps for all Mapping Pixels ... 49
4.4.8. Step 8: Output Maps for Desired Return Periods ... 49
4.5 Discussion of the Liquefaction Triggering Hazard Maps for Utah County ... 53
5. Lateral Spread Mapping ... 55
5.1 Probabilistic Model for Displacement Prediction ... 55
5.2 Performance-Based Lateral Spread Model ... 56
5.3 Probabilistic Lateral Spreading Mapping Procedure ... 58
5.3.1. Step 1: Extract Raster Data at a Map Pixel ... 58
5.3.2. Step 2: Begin Monte Carlo Simulations, Input $T_{15,cs}$ ... 60
5.3.3. Step 3: Input Apparent Loading Value, L ... 62
5.3.4. Step 4: Compute $\log D_H$ ... 66
5.3.5. Step 5: Repeat Steps 2 – 4 for Required Number of Simulations ... 66
5.3.6. Step 6: Develop a D_H Hazard Curve ... 67
5.3.7. Step 7 Repeat Previous Steps for All Mapping Pixels ... 70
5.3.8. Step 8: Output Maps for Desired Return Periods ... 70
5.4 Discussion of the Lateral Spread Hazard Maps for Utah County ... 73
6. Conclusions ... 76
7. Acknowledgements ... 79
8. References ... 80
9. Appendix ... 84

1. Introduction

1.1 Problem Statement

Utah County is the second most-populous county in the state of Utah and comprises a significant portion of the overall state and regional economies. Many state and federal government agencies (e.g., UDOT, National Security Agency (NSA)) and many private industries such as Adobe, Inc. have recently invested billions of dollars in Utah County through the construction of new infrastructure and facilities since 2010. This exciting new growth in Utah County is a major contributor to Utah's better-than-average economy, and is one of the reasons Provo City was voted in 2013 as the #1 Best Place in America for Business and Careers by Forbes Magazine.

However, seismically-induced liquefaction hazard throughout Utah County is generally recognized to be significant due to several factors, including proximity to active seismic sources, proximity to surficial water sources (Utah Lake), high ground water, and relatively high amounts of granular and/or silty soils in the upper 50 feet of sediments. Liquefaction-induced ground failure can cause considerable damage to the built environment during major earthquakes. For example, horizontal displacements due to liquefaction-induced lateral spreading, considered the most pervasive type of liquefaction-induced ground failure, may range from a few tenths of a meter to several meters and are common in liquefaction prone areas (Bartlett and Youd 1992; Youd et al. 2002). The best defense against such damage is identifying areas prone to ground failure and developing planning/development/engineering strategies to mitigate the hazard.

Mapping liquefaction hazard is challenging because for a large area, such as a county, there is considerable spatial and temporal uncertainty in the subsurface conditions and seismic hazard. In addition, liquefaction is a complex phenomenon that is generally modeled empirically based on

case history studies, and the empirical models have large uncertainties. To develop a defensible method for mapping liquefaction hazard, one should account for these significant uncertainties and present the results probabilistically.

1.2 Objectives

The first major objective of the research presented in this report is to develop a new, fully probabilistic procedure for mapping estimates of liquefaction triggering and lateral spread displacement. The procedure uses the best available data, including:

- Available surficial geologic maps
- Available reports on geotechnical investigations
- A digital elevation model (e.g., from aerial lidar measurements or from an even higher-accuracy topographic surveying technique)
- Recent probabilistic seismic hazard analyses from the USGS National Seismic Hazard Mapping Program
- Performance-based liquefaction triggering (Kramer and Mayfield 2007) and lateral spread displacement (Franke and Kramer 2013) techniques
- Recently published empirical liquefaction triggering and lateral spread displacement models

The procedure builds upon the mapping methods developed by Bartlett and Gillins (2013) and Gillins and Bartlett (2013) so that liquefaction hazard mapping can be carried out in areas where geotechnical data is limited and/or lacking.

The second major objective of this report is to use the fully probabilistic procedure to develop liquefaction triggering and lateral spread displacement hazard maps for Utah County, Utah, at return periods of 475, 1033, and 2475 years. The development of probabilistic liquefaction triggering and lateral spread hazard maps provide an important risk assessment tool to agencies, departments, and industries who have recently invested their time and money in Utah County. For example, state departments like the Utah Department of Transportation could use the hazard maps to evaluate their transportation network and to identify potential *problem spots* where performing future site-specific liquefaction studies should be prioritized. Furthermore, probabilistic hazard maps are an invaluable tool when performing emergency/disaster scenario and impact studies.

1.3 Research Tasks

To achieve the proposed objectives of this research, the following research tasks were completed: (1) compiled available geological, geotechnical, and topographical data and developed a GIS database for Utah County, (2) identified the major surficial geological units in the portion of Utah County that is susceptible to liquefaction; (3) developed distributions of geotechnical properties within the major geologic units; (4) developed seismic hazard curves for a series of grid points in the study area based on USGS probabilistic seismic hazard data; (5) interpolated the seismic hazard curves and performed hundreds of thousands of Monte Carlo simulations to develop a distribution of factors of safety against liquefaction triggering and lateral spread displacements every 30 m in the study area; (6) produced new liquefaction triggering and lateral spread displacement maps at return periods of 475, 1033, and 2475 years in Utah County.

1.4 Report Organization

Chapter 2 identifies previous liquefaction hazard mapping in Utah County and provides a brief background on the empirical models selected for mapping liquefaction triggering and lateral spread displacement. Chapter 3 discusses the compilation of the geological, geotechnical, and topographical data and the development of a geodatabase in Utah County. In addition, the chapter identifies major surficial geological units in the study area. Chapter 4 presents distributions of soil properties from the geotechnical database, discusses the development of seismic hazard curves, then shows how these curves were interpolated and input in thousands of Monte Carlo simulations to compute distributions of factors of safety against liquefaction triggering every 30 meters in the study area. The chapter concludes by presenting new liquefaction triggering hazard maps. Chapter 5 proposes the methodology for mapping lateral spreading hazards, then presents new lateral spreading hazard maps in Utah County. Finally, Chapter 6 summarizes the major conclusions of this work.

2. Background

2.1 Previous Mapping Effort in Utah County

Mapping liquefaction hazard for urban areas along the Wasatch Front began in the 1980s, when Utah State University received a National Earthquake Hazards Reduction Program (NEHRP) research grant to assess Davis County (Anderson et al. 1982). Their mapping techniques were further developed and eleven additional counties were mapped, including Utah County in 1986 (Anderson et al. 1994). To produce these maps, Anderson et al. computed the potential for liquefaction triggering at available SPT borehole and CPT sounding locations. They determined critical acceleration values needed to trigger liquefaction using a method introduced by Seed (1979). They then compared these critical accelerations to probabilistic predictions from seismic hazard analyses. Using surficial geologic maps as constraints, they generalized the results at each geotechnical investigation and produced liquefaction potential maps delineating zones of *low*, *moderate*, and *high* liquefaction potential.

Most of the urban areas in Utah County are filled with loosely deposited, saturated lake sediments, and the Anderson et al. (1994) hazard map of Utah County (see Fig. 2.1) shows high liquefaction potential for a significant portion of the county. Although this map is a useful reference, it is desirable to produce new liquefaction hazard maps that show the consequences of liquefaction triggering *and* are based on advancements over the past 30 years in liquefaction hazard evaluation procedures, probabilistic seismic hazard analyses, available and higher-resolution geologic and topographic maps along the Wasatch Front, and the significantly larger number of available SPT and CPT investigations.

The mapping method proposed in this report will build upon the work completed by Olsen et al. (2007) and Gillins (2012). Olsen et al. (2007) compiled a large geospatial database consisting

of thousands of geotechnical investigations in Salt Lake County, geologic maps, and topographic maps to produce a liquefaction-induced lateral spread hazard map for a scenario M7.0 earthquake in Salt Lake County. Gillins (2012) developed a method for mapping the probability of liquefaction triggering and lateral spread displacement exceeding specified thresholds given an event from deaggregation of a probabilistic seismic hazard analysis. This procedure was implemented to map the liquefaction hazard in Weber County, Utah.

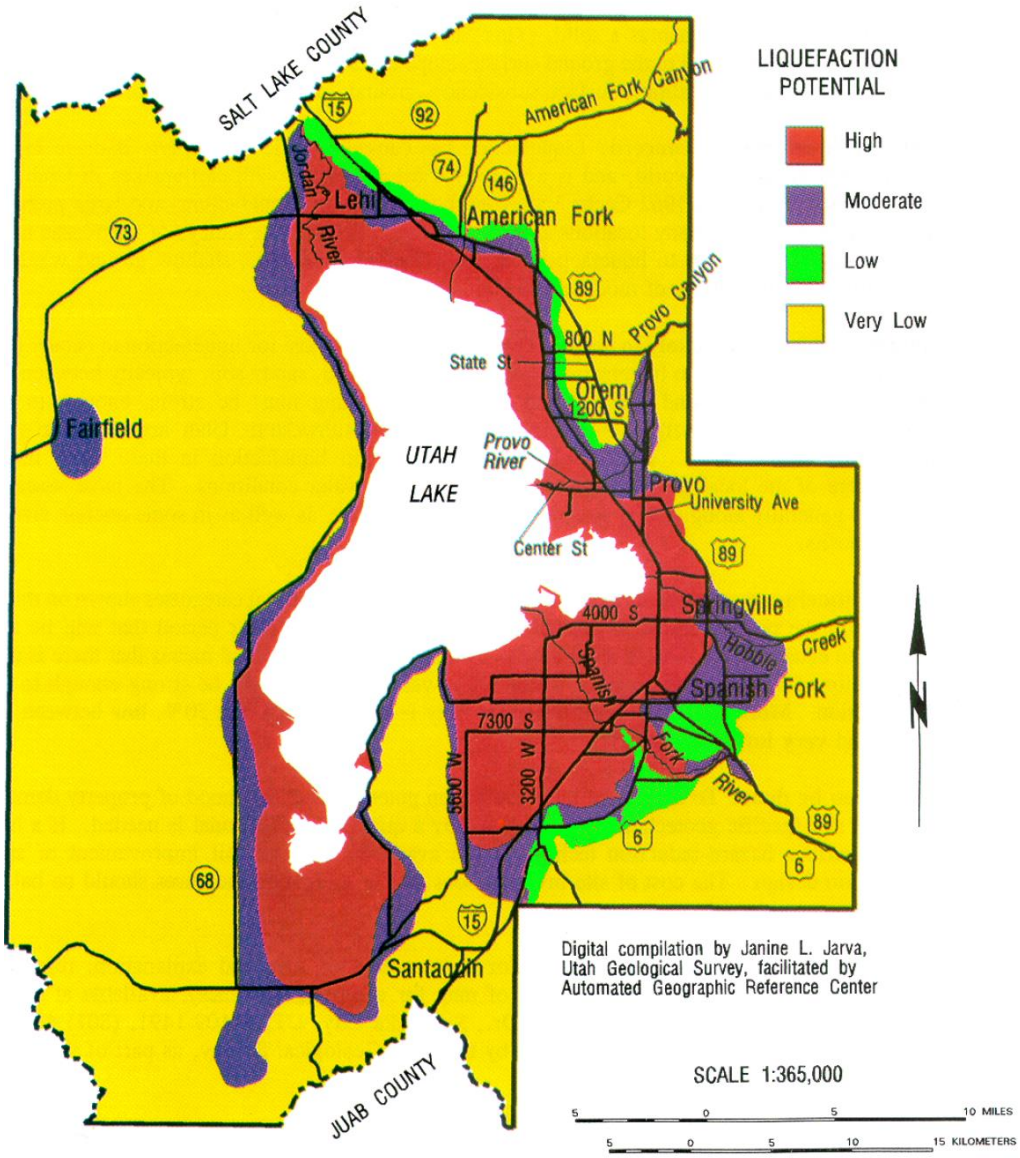

Fig. 2.1. Liquefaction potential hazard map of Utah County, from Anderson et al. (1994)

2.2 Background on Liquefaction Hazard Evaluation

The body of literature and research on liquefaction has continued to grow since the maps of Anderson et al. (1994). This section of the report provides a brief background on some of the state-of-the-art engineering methods for evaluating liquefaction hazard. Many of the equations and methods discussed in this section are commonly used today in engineering consulting offices. Kramer (2008) states that liquefaction evaluations can be grouped into three generic steps: (1) identify which soils are *susceptible* to liquefaction; (2) determine if the earthquake shaking is strong enough to initiate or *trigger* liquefaction in the susceptible soils; (3) if triggering is expected, then estimate the consequences or ground failures (e.g., estimate the horizontal displacement from lateral spreading).

2.2.1 Susceptibility

Regardless of the strength of the earthquake loading, the first step in liquefaction hazard evaluation is to determine if the site contains soils that are *susceptible* to liquefaction. For many years, only sands were considered susceptible to liquefaction. However, lessons learned from earthquakes in California, Idaho, Turkey, Taiwan, and Japan helped to clarify the susceptibility of clays, silts, and gravels. In general, clays are not susceptible to liquefaction, although some have exhibited behavior similar to liquefiable soils during major earthquakes (i.e., cyclic softening). Gravels bounded by layers of soil with low permeability liquefied at lateral spreading case history sites in the 1983 Borah Peak, Idaho, earthquake and the 1995 Kobe, Japan, earthquake (Youd et al. 2002). Silts and sands with high fines contents are quite difficult to classify, because they may or may not be susceptible to liquefaction.

Liquefaction susceptibility is typically judged by many methods, ranging from qualitative to site-specific. Youd and Perkins (1978) compiled a table of criteria based on the type and age of the sedimentary deposit for evaluating liquefaction susceptibility. Youd and Perkins (1978) state that young (< 500 yrs to Holocene) river channels, floodplains, delta, lacustrine, colluvium, dunes, loess, tephra, sebkha, esturine, and uncompacted fill are highly to very highly susceptible to liquefaction. Kramer (1996) presented a method for describing the deposit-level susceptibility using historical, geological, hydrological and compositional criteria.

For more detailed or site-specific analyses, liquefaction susceptibility should be evaluated on a layer-by-layer basis using geotechnical investigations. The first step in susceptibility evaluations are to screen out soils above the ground water table. For pore-water pressures to build up sufficiently during cyclic loading from earthquake shaking, the soil must be saturated or below the ground water table.

Saturated, coarse-grained, cohesionless soils with low fines contents are widely considered susceptible to liquefaction. Clean sands are considered susceptible to liquefaction, and gravelly soils should be considered susceptible if they are bounded by materials with low permeability that allow build-up of excess pore-water pressure. Of course, in a dense state, these soils will not liquefy; however, relative density and its influence on liquefaction is judged when performing the subsequent step of liquefaction triggering analyses.

It is much more difficult to define the susceptibility of soils with high fines contents (e.g., silty sands, clayey sands, sandy silts). After silty soils were observed to have liquefied in several major earthquakes, Seed and Idriss (1982) and Seed et al. (1985) recommended a modified *Chinese criteria* for evaluating the liquefaction susceptibility of fine-grained soils. However, the Chinese

criteria is no longer recommended because it often incorrectly classified liquefied soils as non-susceptible to liquefaction (Bray and Sancio 2006).

Two more-recent studies have provided criteria for evaluating the susceptibility of fine-grained soils. Boulanger and Idriss (2005) reviewed case histories and laboratory tests and identified two types of soil behavior on the basis of stress normalization and stress-strain response. Soils that exhibited *sand-like* behavior were considered susceptible to liquefaction, whereas soils that exhibited *clay-like* behavior were not considered susceptible. Boulanger and Idriss found that soil plasticity can be used to determine if the soil will exhibit sand-like or clay-like behavior, and proposed that the soil is clearly sand-like at a plasticity index (*PI*) less than 3, and a soil is clearly clay-like at a PI greater than 8. Although they noted a transitional phase between 3 and 8, ultimately they recommended that engineers use a conservative guideline with $PI = 7$ as the cutoff between sand-like and clay-like behavior when detailed laboratory testing is not possible. Thus, saturated soils with high fines contents and a $PI < 7$ should be considered susceptible to liquefaction.

After investigating fine-grained soils that liquefied in California, Turkey, and Taiwan, Bray and Sancio (2006) found the ratio of water content to liquid limit (w_c/LL) also influences susceptibility. Bray and Sancio found that soils with $PI < 12$ and $w_c/LL > 0.85$ to be consistently susceptible, and soils with $PI > 18$ or $w_c/LL < 0.80$ to be consistently not susceptible. Transitional soils in-between these two criteria are considered *moderately* susceptible to liquefaction.

The Boulanger and Idriss (2005) model is clearly different than the Bray and Sancio (2006) model. However, both models identify soils that are susceptible to liquefaction or liquefaction-like behavior, and both models are considered valid and defensible for evaluating liquefaction susceptibility.

2.2.2 Triggering

A soil classified as susceptible to liquefaction may not liquefy if the ground shaking is inadequate to overcome the natural liquefaction resistance of the soil. Thus, the next step in liquefaction hazard evaluation is to determine if the cyclic loading produced by earthquake shaking is strong enough to initiate or *trigger* liquefaction in susceptible soils. Evaluating liquefaction triggering involves comparing the cyclic loading with the resistance of the soil to liquefaction. Commonly, this comparison is done using the cyclic shear stress amplitude, expressed in the form of a cyclic stress ratio, *CSR*, for loading and a cyclic resistance ratio, *CRR*, for resistance. The factor of safety against liquefaction, FS_L, is then found by solving Eq. 2.1. If FS_L is less than 1, then liquefaction initiation in the soil is expected.

$$FS_L = \frac{CSR}{CRR} \tag{2.1}$$

To find *CSR*, geotechnical engineers commonly use the *simplified method* proposed by Seed and Idriss (1971), which is expressed as:

$$CSR = 0.65 \frac{a_{\max}}{g} \cdot \frac{\sigma_{vo}}{\sigma'_{vo}} \cdot \frac{r_d}{MSF} \cdot \frac{1}{K_\sigma} \tag{2.2}$$

where a_{max} is the peak ground surface acceleration, g is the acceleration of gravity (in the same units as a_{max}), σ_{vo} is the vertical total stress, σ'_{vo} is the vertical effective stress, r_d is the depth reduction factor that accounts for the dynamic response of the soil profile, *MSF* is the magnitude

scaling factor, and k_σ is the overburden correction factor. Equations for *MSF*, K_σ, and r_d are given later in this section.

The resistance of a soil to liquefaction is known to be directly correlated with its density. Since it is difficult to measure soil density *in situ*, measurements of density are commonly replaced with measurements of penetration resistance from the standard penetration test (SPT) and/or the cone penetration test (CPT). Numerous procedures and correlations have been published and updated over the years for evaluating liquefaction triggering with the SPT or CPT (e.g., Youd et al. (2001); Idriss and Boulanger (2004); Cetin et al. (2004); Moss et al. (2006); Idriss and Boulanger (2008, 2010), Boulanger and Idriss (2012, 2014)).

The Idriss and Boulanger methods are based on an extensive database of case histories of liquefaction and a critical state framework. Some of the case histories in their database involve recent earthquakes in New Zealand and Japan (i.e., the 2010-2011 Canterbury Earthquake Sequence and the 2011 Tohoku, Japan, Earthquake), and the methods have also become quite popular in engineering practice. For these reasons, the authors decided to evaluate the liquefaction triggering hazard in Utah County using the Idriss and Boulanger methods. The remaining section of this report summarizes the recommended equations, and the reader is highly encouraged to read Idriss and Boulanger (2008) and Boulanger and Idriss (2012, 2014) for greater details on the derivation of the equations.

Idriss and Boulanger, as well as many other researchers, have developed SPT-based methods for evaluating liquefaction triggering at a site. Because of its relatively low cost and ruggedness, the SPT is a very popular method for sampling soil and determining the spatial variability of a soil deposit. It is noted that numerous SPTs have been performed in the urban areas of the Wasatch Front in Utah. During an SPT, a borehole is drilled in the ground, and samples of

soil are extracted at discrete depth intervals. During sampling, one counts the number of required blows (*N*) with a 140 lb. hammer falling freely 30 in. to drive a standard split-spoon sampling tube (i.e., 2 in. outside diameter, 1 3/8 in. inside diameter) the final 12 in. of an 18 in. sample length. The SPT blow count value, N_m, is low in loose soils, and is increasingly higher in increasingly denser soils. Thus, N_m can be used as an index of a soil's *in situ* density, and it has been correlated with a large number of engineering characteristics (e.g., Kulhawy and Mayne 1990).

For SPT-based methods, Boulanger and Idriss (2012) used a maximum likelihood approach to develop a probabilistic version of their SPT liquefaction triggering correlation. The recommended correlation for CRR is expressed as:

$$CRR = \exp\left\{ \frac{(N_1)_{60cs}}{14.1} + \left[\frac{(N_1)_{60cs}}{126}\right]^2 - \left[\frac{(N_1)_{60cs}}{23.6}\right]^3 + \left[\frac{(N_1)_{60cs}}{25.4}\right]^4 - 2.67 + \varepsilon_{\ln(R)} \right\} \tag{2.3}$$

where $(N_1)_{60cs}$ is the clean-sand equivalent SPT blow count number, and $\varepsilon_{ln(R)}$ is the error of the model which is normally distributed with a mean of 0.0 and a standard deviation = 0.13.

Idriss and Boulanger (2008, 2010) summarize equations for correcting raw N_m values from an SPT borehole log to $(N_1)_{60cs}$ values. Idriss and Boulanger used these equations to analyze the liquefaction case histories in order to ultimately develop the model shown in Eq. 2.3; thus, these equations should be used when applying Eq. 2.3. First, N_m is corrected to $(N_1)_{60}$ by the following relationship:

$$(N_1)_{60} = C_E C_B C_R C_S C_N N_m \tag{2.4}$$

where C_E is the energy ratio correction factor accounting for the high variability in the amount of energy delivered to the drill rod stem by each impact of the SPT hammer, C_B is a correction factor for the borehole diameter, C_R is a correction factor for rod length, C_S is a correction factor for a sampler that had room for liners but was used without liners, and C_N is the overburden correction meant to account for the effects of increasing confining stress. Table 2.1 presents recommended values in Idriss and Boulanger (2008) for C_E, C_B, C_R, and C_S.

A number of different relationships have been proposed for C_N, and Idriss and Boulanger (2010) recommended the following:

$$C_N = \left(\frac{P_a}{\sigma'_{vo}} \right)^{0.784 - 0.0768\sqrt{(N_1)_{60cs}}} \leq 1.7 \tag{2.5}$$

where σ'_{vo} is the vertical effective stress. As shown, $(N_1)_{60cs}$ is on the right side of Eq. 2.5, thus C_N must be found by iteration. The limit of 1.7 on the maximum value of C_N is only reached when σ'_{vo} is less than 35 kPa (which would generally occur at shallow depths less than 2 m).

Numerous papers report that a soil with high fines content is more resistant to liquefaction than a soil with low fines content (e.g., Youd et al. 2001; Cetin et al. 2004). Thus, for liquefaction triggering evaluations, $(N1)_{60}$ values need to be corrected to *clean-sand equivalent* values (i.e., $(N1)_{60cs}$). Idriss and Boulanger (2008) presented the following models for making this conversion, which show the apparent increase in $(N_1)_{60}$ for liquefaction triggering analyses as a result of increasing fines content:

$$(N_1)_{60cs} = (N_1)_{60} + \Delta(N_1)_{60cs} \tag{2.6}$$

$$\Delta\left(N_1\right)_{60cs} = \exp\left(1.63 + \frac{9.7}{FC+0.01} - \left(\frac{15.7}{FC+0.01}\right)^2\right) \tag{2.7}$$

where *FC* is the percent fines content or the percentage of soil passing the No. 200 standard sieve.

Table 2.1. Recommended factors in Idriss and Boulanger (2008) for correcting N_m to $(N_1)_{60}$

Factor	**Description**
C_E, energy ratio	Empirical estimates for C_E involve considerable uncertainty. A range of values is possible according to the hammer release type • Doughnut hammer: C_E = 0.5 to 1.0 • Safety hammer: C_E = 0.7 to 1.2 • Automatic triphammer: C_E = 0.8 to 1.3
C_B, borehole diameter	<u>Borehole diameter</u> <u>Recommendation</u> • 65 – 115 mm (2.5 to 4.5 in.): C_B = 1.0 • 150 mm (6 in.): C_B = 1.05 • 200 mm (8 in.): C_B = 1.15
C_R, rod length	<u>Rod length</u> <u>Recommendation</u> • < 3 m: C_R = 0.75 • 3 – 4 m: C_R = 0.80 • 4 – 6 m: C_R = 0.85 • 6 – 10 m: C_R = 0.95 • 10 – 30 m: C_R = 1.00
C_s, sampler liner	• Standard split-spoon sampler without room for liners (i.e., the inside diameter is a constant 1 3/8 in.): C_s = 1.0 • Split-spoon sampler with room for lines but with the liners absent: $C_S = 1.1$ for $\left(N_1\right)_{60} \le 10$ $C_s = 1 + \frac{(N_1)_{60}}{100}$ for $10 \le \left(N_1\right)_{60} \le 30$ $C_s = 1.3$ for $\left(N_1\right)_{60} > 30$

Idriss and Boulanger (2008) also provided models for estimating r_d and K_σ. Based on several hundred parametric site response analyses, r_d is found by the following recommended expression:

$$r_d = \exp(\alpha + \beta \cdot M) \tag{2.8}$$

where α and β are a function of z, the depth in meters (as expressed below), and M is the earthquake moment magnitude.

$$\alpha = -1.012 - 1.126 \sin(\frac{z}{11.73} + 5.133) \tag{2.9}$$

$$\beta = 0.106 + 0.118 \sin(\frac{z}{11.28} + 5.142) \tag{2.10}$$

The recommended relationship for K_σ is computed as:

$$K_\sigma = 1 - C_\sigma \ln\left(\frac{\sigma'_{vo}}{P_a}\right) \leq 1.1 \tag{2.11}$$

where the coefficient C_σ can be found in terms of corrected SPT penetration resistance by:

$$C_\sigma = \frac{1}{18.9 - 2.55\sqrt{(N_1)_{60cs}}} \leq 0.3 \tag{2.12}$$

Recently, Boulanger and Idriss (2014) recommended a new relationship for *MSF* in order to account for varying soil characteristics. Idriss and Boulanger reprocessed the SPT-based liquefaction triggering case history database using this new *MSF* relationship, and the results were in good agreement with their SPT-based triggering curve (Eq. 2.3). Thus, the currently recommended *MSF* relationship is:

$$MSF = 1 + (MSF_{\max} - 1)\left(8.64 \cdot \exp\left(\frac{-M}{4}\right) - 1.325\right) \tag{2.13}$$

where MSF_{max} is correlated with $(N_1)_{60cs}$ by the following expression:

$$MSF_{\max} = 1.09 + \left(\frac{(N_1)_{60cs}}{31.5}\right)^2 \leq 2.2 \tag{2.14}$$

Using the equations presented in this section of the report, one may solve for *CSR*, *CRR*, and FS_L for each layer of soil susceptible to liquefaction at a project site. Although it is possible to calculate these values for each layer, researchers that developed liquefaction triggering models generally computed a single *CSR* and *CRR* value for a case history site. For example, when evaluating case histories of liquefaction triggering, Idriss and Boulanger first identified the *critical layer* at a site, or the layer with the greatest likelihood of triggering during the earthquake shaking. They then computed *CSR*, *CRR*, and $(N_1)_{60cs}$ for the critical layer at each case study site in their database and then fit the triggering curve (Eq. 2.3) to the results. To be consistent with this approach, when mapping the liquefaction triggering hazard, the probability of liquefaction at a

certain location can be computed by finding FS_L for the *critical layer* of soil at the location, or at that layer with the greatest likelihood for triggering.

2.2.3 Consequence - Lateral Spreading

Triggering analyses are vital for evaluating the liquefaction hazard at a site. Of course, ground failures due to liquefaction are impossible if the earthquake shaking is not strong enough to trigger liquefaction in susceptible soils. However, if the shaking were strong enough, then the methods described in the previous section of this report do not provide an indication of the consequences of liquefaction triggering. Hence, the next step in the hazard evaluation is to assess the consequences if liquefaction were to trigger at a site.

There are a large number of possible consequences or ground failures due to liquefaction, including loss of bearing strength, ground oscillation, settlement due to the ejection of material from the liquefied layer, lateral spreading, and flow failure. Although many of these failures are problematic, the most pervasive type of liquefaction-induced ground failure is lateral spreading (NRC 1985). During lateral spreading, mostly intact blocks of soil above the liquefied layer may displace down gentle slopes or towards free-faces (e.g., a river channel or steep topographic depression). These horizontal displacements may result in considerable damage to bridges, buildings, pipelines, roadways, and other constructed works.

Numerous models have been developed for predicting the amount of horizontal displacement due to lateral spreading at potentially liquefiable sites (e.g., Hamada et al. (1986), Youd and Perkins (1987), Bartlett and Youd (1995), Rauch and Martin (2000), Youd et al. (2002), Bardet et al. (2002), Zhang et al. (2004), Faris et al. (2006), and Gillins and Bartlett (2013)). The Youd et al. (2002) multilinear regression model is widely popular for engineering practice, and it

is based on earthquake source, topographical, and soil gradation factors that were shown to be statistically significant in estimating the amount of liquefaction-induced lateral spread displacement at liquefied sites.

Unfortunately, the Youd et al. (2002) model requires certain inputs, namely mean grain sizes and fines contents, which were rarely reported on available SPT logs in Utah. As a result, Gillins and Bartlett (2013) modified the Youd et al. (2002) model by replacing the mean grain size and fines content variables with soil type descriptors. Gillins and Bartlett (2013) showed that the statistical performance of this modified model was only slightly worse than the Youd et al. (2002) model. In addition, this modification enabled the mapping of the lateral spreading hazard in Weber County, Utah (Gillins 2012; Bartlett and Gillins 2013). The Gillins and Bartlett (2013) model is summarized in this section because it will be used to map the lateral spreading hazard in Utah County.

Gillins and Bartlett (2013) developed the following multilinear regression model:

$$\begin{aligned} logD_H = b_0 + b_1 M + b_2 LogR^* + b_3 R + b_4 LogW + \\ + b_5 LogS + b_6 LogT_{15,cs} + 0.252 + \varepsilon \end{aligned} \tag{2.15}$$

where D_H is the estimated horizontal displacement (m) from lateral spreading; M is the moment magnitude of the earthquake; R is the nearest horizontal or mapped distance from the site to the seismic energy source (km); W is the ratio of the height of the free face to the horizontal distance between the base of the free face and the point of interest (%); S is the ground slope (%); ε is the error of the model, defined below; and R^* is found by Eq. 2.16.

$$R^* = R + 10^{0.89 \cdot M - 5.64} \tag{2.16}$$

$T_{15,cs}$, the only geotechnical variable in Eq. 2.15, is defined as:

$$T_{15,cs} = T_{15} \cdot 10 \wedge \left(\frac{-0.683 \cdot x_1 - 0.200 \cdot x_2 + 0.252 \cdot x_3 - 0.040 \cdot x_4 - 0.535 \cdot x_5 - 0.252}{0.592} \right) \tag{2.17}$$

where T_{15} is the cumulative thickness (m) of saturated soil susceptible to liquefaction with corrected SPT blows counts, $(N_1)_{60} \leq 15$, and x_i is the thickness of the layers in the site profile that comprise T_{15} with $SI = i$ divided by T_{15}. In order to apply Eq. 2.15, a practitioner must first assign a soil index (*SI*) to each layer susceptible to liquefaction at the site. The soil index (*SI*) for each layer is assigned using its soil description on a borehole log and the *SI* definitions in Table 2.2.

Using the Youd et al. (2002) lateral spreading case history database, Gillins and Bartlett (2013) regressed a set of coefficients for Eq. 2.15. These coefficients are given in Table 2.3 according to the topographic conditions at a site. The error for the regression model, ε, is normally distributed with a mean of 0.0 and a standard deviation = 0.2232.

Table 2.2. Soil indices and their definitions.

SI	Definition
1	Silty gravel with sand, silty gravel, fine gravel
2	Coarse to very coarse sand, sand and gravel, gravelly sand
3	Sand, medium to fine sand, sand with some silt
4	Fine to very fine sand, sand with silt, silty sand, dirty sand
5	Sandy silt, silt with sand
6	Non-liquefiable such as cohesive soil or soil with high plasticity

Table 2.3. Regression coefficients for the Gillins and Bartlett (2013) empirical lateral spread model.

Model	b_0	b_1	b_2	b_3	b_4	b_5	b_6
Ground - Slope	-8.208	1.318	-1.073	-0.016	0	0.337	0.592
Free Face	-8.552	1.318	-1.073	-0.016	0.445	0	0.592

3. Data Compilation

The liquefaction triggering and lateral spreading hazard mapping methods proposed in this report rely on surficial geology base maps, available geotechnical investigations, and a digital elevation model (DEM) for identifying ground slopes and the height and proximity to free-faces. This chapter discusses the compilation and source of the geological, geotechnical, and topographical data in Utah County. All of the data discussed in this chapter were stored in a geodatabase file that can be downloaded from the first author's website.

3.1 Geological Mapping

A vector-based surficial geology base map of the study area (Constenius et al. 2011) was obtained from the Utah Geological Survey and input into a geographic information system (GIS). The Constenius et al. (2011) map is a compilation of detailed new mapping of several 7.5-minute quadrangles at 1:24,000 to 1:50,000-scale along part of the populous Wasatch Front and Utah Valley. Overall, the map provides the surficial geology for the entire 30 minute by 60 minute Provo quadrangle; however, only the west 1/3 of this map was needed for the study area. Fig. 3.1 presents the study area in Utah County, and shows the surficial geologic units from the Constenius et al. (2011) map. The study area is filled primarily with Holocene to Upper Pleistocene alluvial, lacustrine, and deltaic deposits. According to Youd and Perkins (1978), these deposits are generally moderately to very highly susceptible to liquefaction. Fig. 3.1 also depicts the Wasatch Mountains which bound the study area on the east, the Utah segment of the Wasatch Fault Zone (the primary seismic threat in Utah County), the extents of Utah Lake, and West Mountain to the south of Utah Lake. Although not shown in Fig. 3.1, the study area is also bounded on the west by the Lake Mountains.

The authors grouped the quaternary surficial geologic units in the study area into 14 categories: stream alluvium, stream-terrace alluvium, old alluvial fans, young alluvial fans, delta, fine-grained lacustrine, coarse-grained lacustrine (lacustrine sand), mass movements (landslides), lacustrine gravel, mixed alluvial-fan and delta, human disturbance, mixed lacustrine and alluvium, mixed alluvial fan and terrace, and mixed alluvium and colluvium. Table 3.1 defines the 14 categories and provides a description and age for the units from the Constenius et al. (2011) map.

The mountains are not considered susceptible to liquefaction as their deposits are generally very dense and they generally have a very deep groundwater table.

3.2 Geotechnical Database

Available geotechnical investigations were collected, digitized, and stored in a geospatial database. The collection of Utah County SPT borehole logs and CPT soundings required the participation of multiple engineering firms and their clients, as well as government agencies like the Utah Department of Transportation (UDOT), Utah Geological Survey (UGS), Central Utah Water Conservancy District (CUWCD), as well as local city governments. Letters from private entities addressed to its former geotechnical engineering consultants that requested the release of all geotechnical subsurface information (SPT borehole logs, CPT soundings, shear wave velocity profiles, and test pits) to the research group aided the data collection.

Data from available SPT and CPT records were input into a Microsoft Access database that was developed and explained by members of the research team during a previous liquefaction hazard mapping study in Weber County, Utah (Bartlett and Gillins 2013). Tables A1-A4 in the appendix provide specific information on each of the data fields in the database. The SPT boring logs provided soil descriptions and classifications, layer delineations, and uncorrected SPT blow

counts (N_m). Additionally, some of the logs reported lab measurements on collected soil samples, such as fines contents, Atterberg limits, unit weights, and moisture contents. Most of the logs reported the depth to ground water if it was encountered. The CPT soundings provided measurements of friction ratio, sleeve friction, cone-tip resistance, and pore water pressure. Most of the CPT soundings also had a pore-water pressure dissipation test data that gave an estimation of the depth of groundwater.

To quantify the quality of the data, a ranking was assigned to each measured soil property. A "1" was assigned to data that was found on the original test record. A "2" was assigned if the information could be estimated from a nearby test in the same report. A "2" was also assigned to ground water depths that were not measured at completion. A "3" was assigned if the data was less certain--most often because the information was inferred from another report on another nearby test log.

Overall, 753 borehole logs and 39 CPT soundings in the study area were collected, digitized, and stored in the database. Fig. 3.1 shows the spatial location of each SPT. As can be seen, the data is spaced relatively well throughout the study area and numerous tests are shown along the I-15 corridor; however, some portions of the county with limited development (west and just southeast of Utah Lake) have few investigations.

Table 3.1 shows the number of SPT borehole logs in each of the 14 major geologic units in the study area. All 753 logs were used for characterizing the typical soil properties (e.g., moisture content, Atterberg limits, unit weights) for the geologic units; however, a large number of the tests (329) were quite shallow, and there was concern that some tests may not have encountered all of the liquefiable layers at deeper depths. As a result, only tests that extended beyond at least a depth of 20 ft. were used when mapping the liquefaction triggering and lateral

spreading hazards. Table 3.1 shows SPT logs greater than 20 ft. in all 14 major geologic units in the study area. A large number of SPT logs are available for the common units that cover the majority of the study area (e.g., Qafy, Qlf, Qfdp, Qls). Of course, some of the other units have a very small number of SPT logs (e.g., Qms, Qat, Qd); however, this lack of sampling is because these units are rare in the study area.

Future tests in under-developed portions of the study area, or in the major geologic units with limited testing would undoubtedly improve the accuracy of the hazard maps. Hopefully, future tests can be easily added to the Utah County geotechnical database, and new maps can be readily produced that refine the maps presented in this report.

3.3 Topographical Data

In more recent liquefaction hazard mapping efforts in Utah (e.g., Olsen et al. (2007), Bartlett and Gillins (2013)), researchers constructed digital elevations models from the USGS National Elevation Dataset. Although this was the best available topographical data at the time, these DEMs were generally at a coarse resolution of 10 – 30 meters. However, in the fall of 2013 and spring of 2014, the Utah Automated Geographic Research Center (AGRC) and partners acquired highly-resolute aerial lidar data for urban areas in Salt Lake and Utah Counties. The aerial lidar data was filtered to produce a bare-earth digital elevation model with a resolution of 0.5 meters. Such a rich, highly-resolute source of topographical data is extremely helpful for identifying steep slopes, free faces, etc. in order to map the lateral spread hazard in Utah County.

The lidar-derived digital elevation model of the study area was downloaded from the AGRC and was stored in the GIS for this project (from http://gis.utah.gov/data/elevation-terrain-

data/2013-2014-lidar/). As explained in Chapter 5, it was used for estimating ground slopes and free face ratios while mapping the lateral spreading hazard.

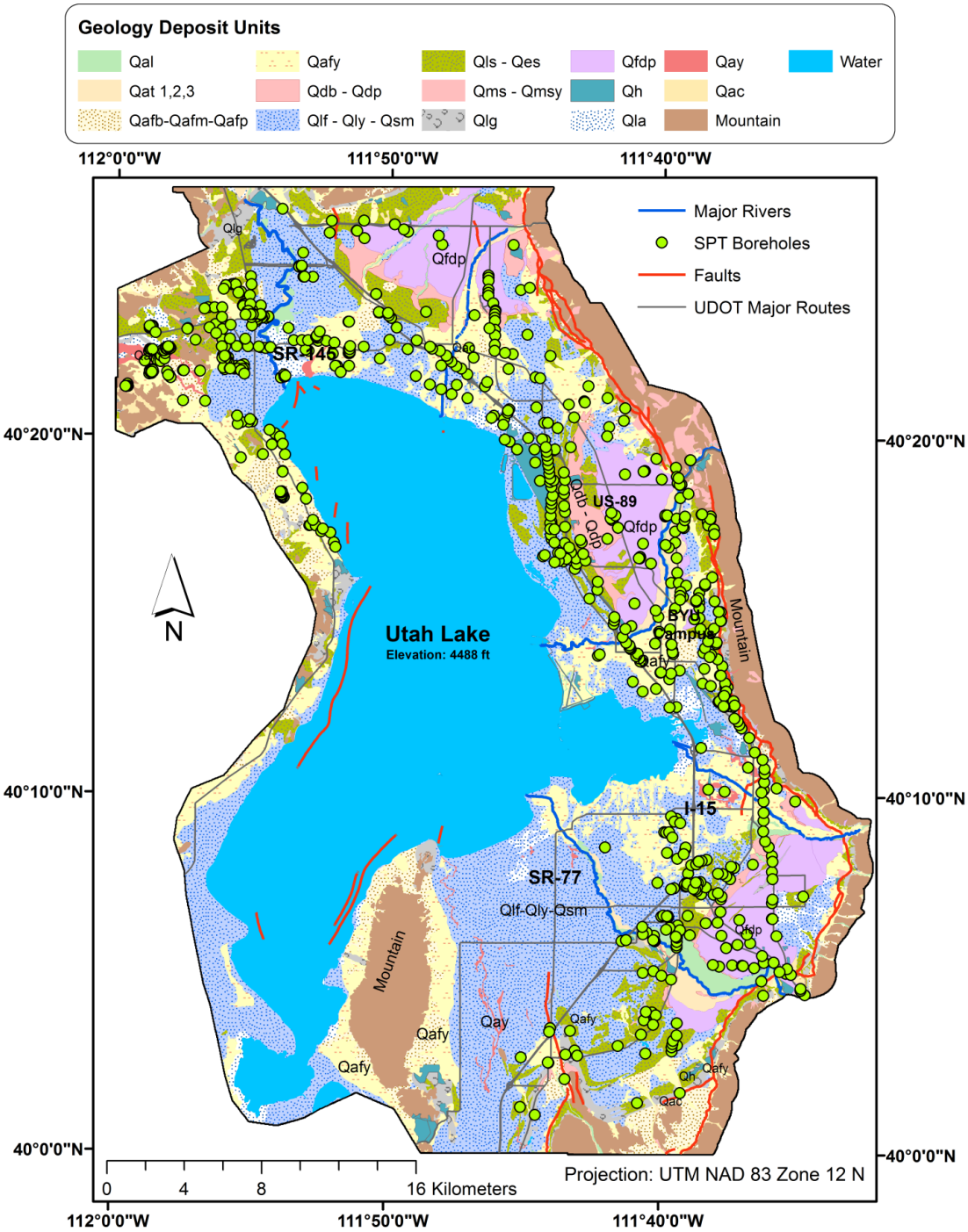

Fig. 3.1. Surficial geology and location of SPT boreholes in the study area, Utah County, Utah (See Table 3.1 for a description of the 14 geologic categories)

Table 3.1. Geologic units in study area, descriptions, approximate age, and number of SPT logs.

Deposit Symbol	Description	Age*	#SPT†
1. Stream Alluvium			
Qal	Modern stream alluvium	H	20 (33)
2. Stream-Terrace Alluvium			
Qat_1	Stream-terrace alluvium, lowest terrace levels	H - UP	4 (7)
Qat_2	Stream-terrace alluvium, medium terrace levels	H - UP	2 (4)
Qat_3	Stream-terrace alluvium, highest terrace levels	H - UP	0 (1)
3. Alluvial Fan – Old			
Qafb	Transgressive (Bonneville) Lake Bonneville-age	UP	0 (1)
Qafm	Intermediate Lake Bonneville-age alluvial fan	UP to middle P	6 (21)
Qafp	Regressive (Provo) Lake Bonneville-age alluvial fan	UP	3 (10)
4. Alluvial Fan – Young			
Qafy	Younger alluvial-fan	H	98 (171)
5. Delta			
Qdb	Near Bonneville shoreline of Lake Bonneville	UP	1 (1)
Qdp	Near and below Provo shoreline of Lake Bonneville	UP	5 (13)
6. Fine-Grained Lacustrine			
Qlf	Fine-grained lacustrine from Lake Bonneville	UP	100 (194)
Qly	Young lacustrine less than 6 m thick and overlies Qlf unit	H– UP	4 (6)
Qsm	Fine, organic-rich sediment from springs, marshes, seeps; less than 3 m thick and overlies Qlf unit	H– UP	1 (1)
7. Lacustrine Sand			
Qls	Lacustrine sand below Bonneville and Provo shorelines	UP	58 (100)
Qes	Eolian sand; 1-1.5 m thick and derived from Qls unit	H - UP	4 (7)
8. Landslides			
Qmsy	Modern landslide, currently or recently active	H	3 (6)
Qms	Modern landslide	H	2 (2)
9 – 14. Others			
Qlg	Lacustrine gravel and sand near Bonn. and Provo shorelines	Uppermost P	15 (21)
Qfdp	Lake Bonneville alluvial-fan and delta, Provo stage	Uppermost P	33 (61)
Qh	Human disturbance – fill for major interstate and highways	Historic	45 (53)
Qla	Lacustrine and alluvial, undivided	H – UP	14 (20)
Qay	Alluvial fan and terrace post-Provo shoreline of Lake Bonn.	H – UP	3 (13)
Qac	Alluvium and colluvium, undivided	Quaternary	3 (7)

* = UP = Upper Pleistocene; P = Pleistocene; H = Holocene

† = Number in parenthesis is the grand total of SPTs in the unit. Number outside of parenthesis is the total of SPTs with maximum test depths greater than 20 ft.

4. Liquefaction Triggering Mapping

After determining that the soil at a site is susceptible to liquefaction, numerous inputs are required in order to estimate the factor of safety against liquefaction triggering using the simplified method outlined in Chapter 2. Unfortunately, several of these inputs have considerable uncertainty, including: (1) uncertainty in the subsurface characterization, which can be very large at locations with limited, sparse, or crude geotechnical investigations; (2) error in the empirical liquefaction triggering model employed in the evaluation, (e.g., $\varepsilon_{ln(R)}$, defined in Chapter 2); and (3) uncertainty in the seismic ground motion, which can be expressed by a probabilistic seismic hazard analysis (PSHA) at the site of interest.

Because of the large uncertainty, it is prudent to develop a fully probabilistic method for mapping the liquefaction triggering hazard—especially when attempting to map a regional area using available data. Using data discussed in Chapter 3, this chapter presents a method aimed to model these three major sources of uncertainty in order to estimate the return period of liquefaction triggering. This method was then implemented to map the liquefaction triggering hazard at return periods of 475, 1033, and 2475 years in the study area in Utah County.

4.1 Analysis of SPT Boreholes in the Utah County Geotechnical Database

The geotechnical database is useful for developing distributions of expected soil properties for each mapped geologic unit in the study area. These distributions can be used to model the uncertainty in the subsurface characterization. For example, assuming an adequate number of standard penetration tests were performed in each major unit, it is possible to develop a distribution of expected $(N_1)_{60cs}$ values for critical layers susceptible to liquefaction in each unit. The $(N_1)_{60cs}$

distributions could then be input in Eq. 2.3 to compute a distribution of *CRR* at sites of interest in a geologic unit in the study area.

Distributions of soil properties for each geologic unit were developed by evaluating the results of the SPT logs in the Utah County geotechnical database. As mentioned in Chapter 2, there was concern that many of the shallow logs in the database may not have encountered all of the liquefiable layers at deeper depths. Thus, only for those logs that extended to at least a depth of 20 ft., the goal was to first, identify all soil layers susceptible to liquefaction; then, correct raw N_m values to $(N_1)_{60}$ and $(N_1)_{60cs}$ using Eq. 2.4 and Eq. 2.7 for each identified layer. Unfortunately, as is often the case, the majority of the SPT logs did not provide the moisture content, unit weight, fines content, and Atterberg limits for *every* layer. In addition, most of the SPT logs did not list a measured value for the energy ratio correction factor, C_E, which is highly variable depending on the hammer release type, per Table 2.1. These data are needed for liquefaction susceptibility analyses, and for correcting N_m to $(N_1)_{60cs}$ for liquefaction triggering analyses.

To model this missing data and account for its uncertainty, Monte Carlo simulations were performed where a value was first input for C_E depending on the hammer release type, and value(s) were also input for those layers missing a measurement of moisture content, fines content, and/or dry unit weight. Then, N_m values were corrected to $(N_1)_{60}$ and $(N_1)_{60cs}$ for all layers considered susceptible to liquefaction. The simulations were repeated 300 times until a distribution of $(N_1)_{60}$ and $(N_1)_{60cs}$ values were computed for each susceptible layer at each SPT. Bartlett and Gillins (2013) found that this number of simulations was adequate to fully model the uncertainties in the inputs.

Prior to performing the simulations, distributions of moisture contents, fines contents, and unit weights were developed using measurements recorded on *all* of the SPT logs in the database

(i.e., including the shallow logs). As expected, the distributions for these properties varied by soil type. Thus, for every layer on each SPT log, a soil index value (*SI*) was assigned per Table 2.2. Figs. 4.1 - 4.3 show histograms of dry unit weights, moisture contents, and fines contents, respectively, grouped according to *SI*. It was also discovered that nearly all of the soils with SI = 6 had a plasticity index greater than 7, and almost all of the silts, sandy silts, and silty sands (i.e., SI = 4 or 5) had a plasticity index less than 7 in the database. For conservatism and following recommendations in Boulanger and Idriss (2005), the authors decided to consider saturated layers with $SI \leq 5$ susceptible to liquefaction. Layers with SI = 6 were screened out from all further liquefaction hazard analyses since their plasticity index was nearly always greater than 7.

In addition to computing the histograms in Figs. 4.1 – 4.3, distributions were developed for C_E depending on the hammer release type. Per Table 2.1, C_E may vary from 0.7 to 1.2 for a safety hammer, and from 0.8 to 1.3 for an automatic triphammer. (Note none of the SPT data in the database involved doughnut hammers.) Assuming that these ranges of values are normally distributed, then a mean value for each hammer type was computed, and the standard deviation (σ_{CE}) was estimated to equal one-sixth of the range. Setting the standard deviation to equal one-sixth of the range seems reasonable because for a normally distributed random variable, 99.7% of the data is within ± 3 standard deviations of the mean. Thus, for the safety hammer, the mean of its distribution was set to equal 0.95 with σ_{CE} = 0.08; for the automatic triphammer, the mean was set to equal 1.05 with σ_{CE} = 0.08.

All of the aforementioned distributions were used in the Monte Carlo simulations at each SPT. For a single simulation, if a layer lacked a moisture content measurement on the SPT log, then a moisture content was randomly selected from the distribution depicted in Fig. 4.2. Any other missing data for each layer was also randomly selected using the distributions in Figs 4.1 –

4.3. Depending on the hammer release type, a value for C_E was also randomly selected using the Matlab function *randn*. This function generates a normally distributed random number with a user-defined mean and standard deviation. After filling in the missing data on the SPT log using the random sampling, the total and effective stress profiles were computed, and N_m was corrected to $(N_1)_{60}$ and $(N_1)_{60cs}$ using equations presented in Chapter 2. Lastly, for future lateral spread hazard mapping purposes, $T_{15,cs}$ was computed for each simulation per Eq. 2.17. This process was then repeated 300 times for each SPT of sufficient depth.

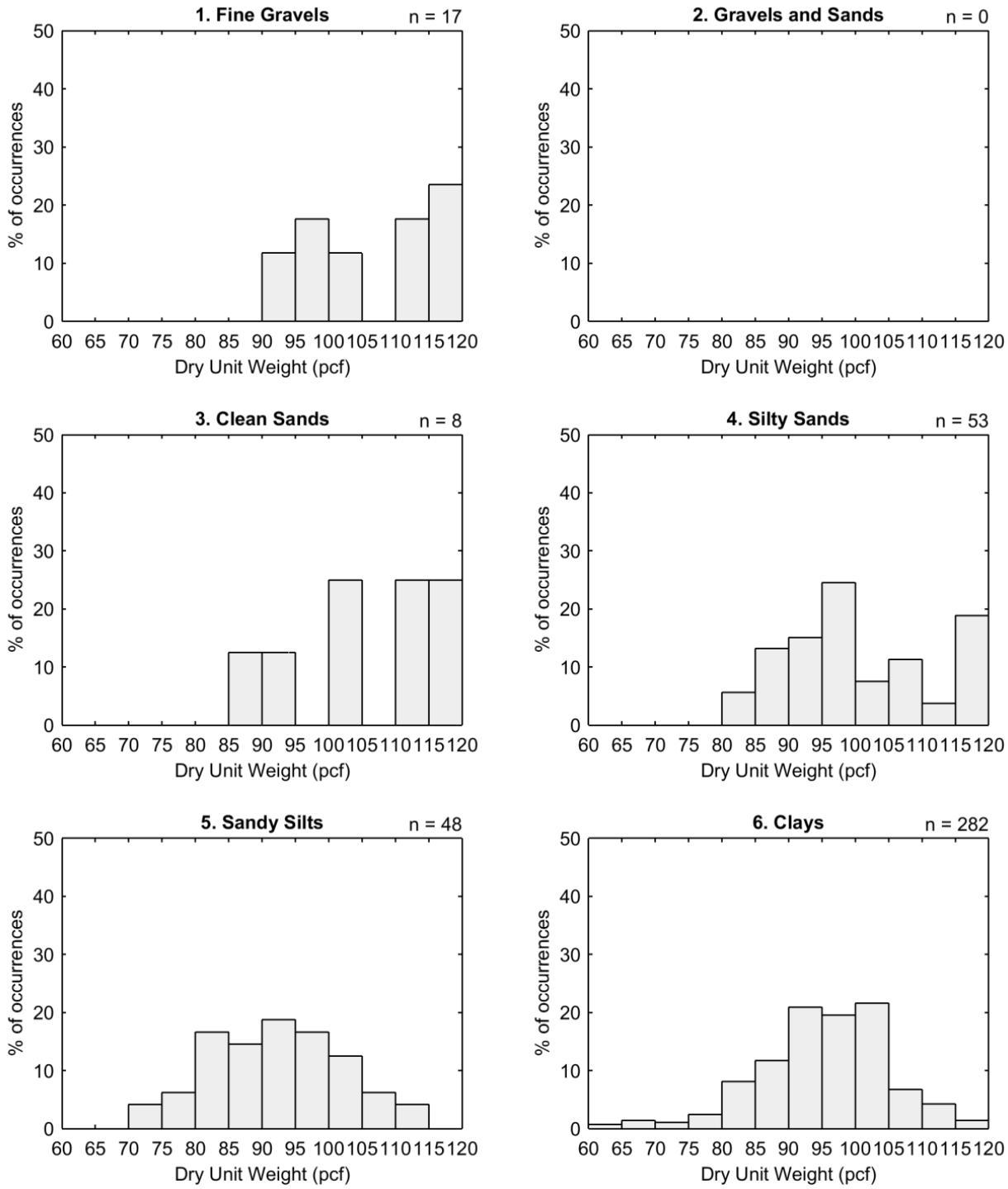

Fig 4.1. Histograms of measured dry unit weight (in pounds per cubic foot) for layers classified as *SI* = 1 to 6, Utah County geotechnical database.

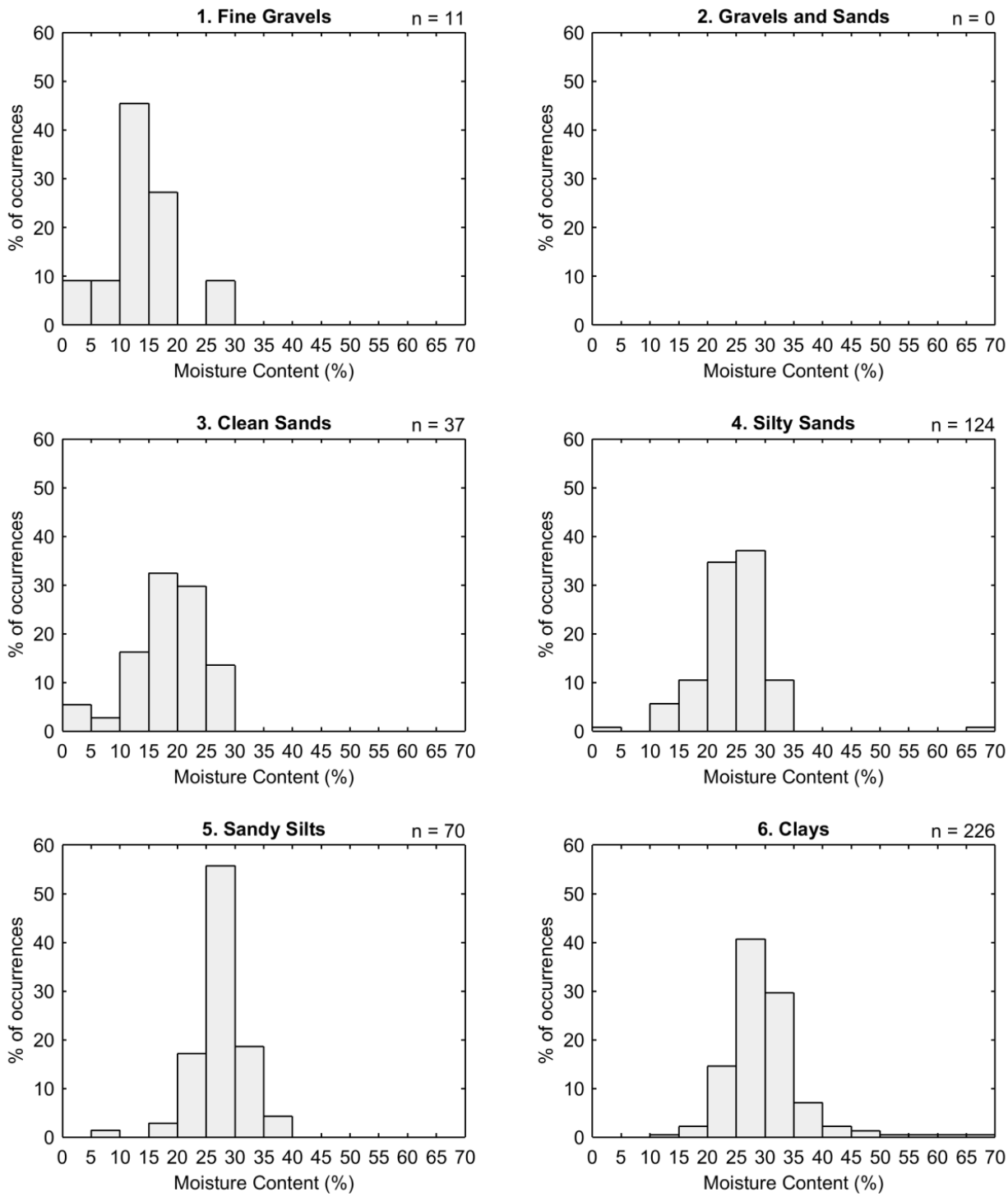

Fig 4.2. Histograms of measured moisture content (in percent) for layers classified as *SI* = 1 to 6, Utah County geotechnical database.

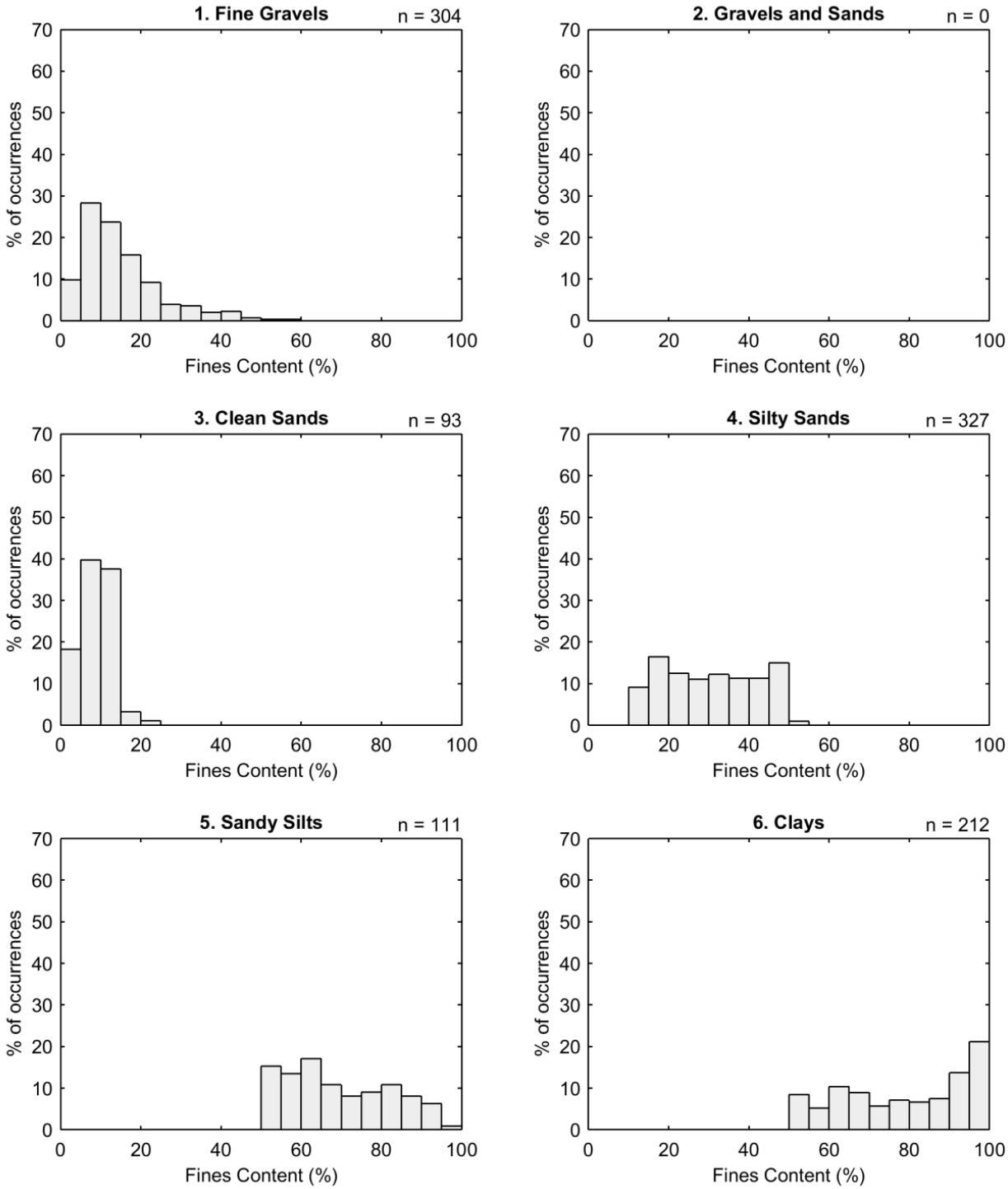

Fig 4.3. Histograms of measured fines content (in percent) for layers classified as *SI* = 1 to 6, Utah County geotechnical database.

4.2 Performance-Based Liquefaction Triggering Model

In order to produce fully probabilistic liquefaction triggering maps, one must model the significant uncertainties in the seismic hazard. Probabilistic seismic hazard analyses (PSHA) examine the distribution and combinations of magnitude and distance to all known seismic sources that may produce significant shaking at a site of interest. Kramer and Mayfield (2007) explained how to model all of the earthquake magnitudes that contribute to the seismic hazard at a site of interest using a performance-based engineering framework developed by the Pacific Earthquake Engineering Research Center (PEER). The PEER framework enables the computation of risk, which can be expressed in the form of an engineering demand parameter (*EDP*), as a function of earthquake ground shaking expressed in the form of an intensity measure (*IM*). The mean annual rate of non-exceedance (Λ) of a selected engineering demand parameter (*edp*), given an earthquake intensity measure, is expressed as:

$$\Lambda_{edp} = \sum_{i=1}^{N_{IM}} P(EDP < edp \mid IM = im_i)\Delta\lambda_{im_i} \tag{4.1}$$

where $\Delta\lambda_{imi}$ is the increment of intensity measure hazard, and P($EDP < edp \mid IM = im_i$) is the probabilistic response model that relates *EDP* to *IM*.

Kramer and Mayfield (2007) explained that for liquefaction triggering, FS_L represents the *EDP*, and a_{max} and *M* represent the earthquake *IM*. Combining the probabilistic version of computations for FS_L (e.g., from Eqs. 2.1-2.3) with the results of a seismic hazard analysis enables computation of the mean annual rate of non-exceedance of a selected factor of safety, FS_L^*, by:

$$\Lambda_{FS_L^*} = \sum_{j=1}^{N_M} \sum_{i=1}^{N_{a_{\max}}} P[FS_L < FS_L^* \mid a_{\max,i}, m_j] \Delta\lambda_{a_{\max,i}, m_j} \tag{4.2}$$

where N_m and N_{amax} = number of magnitude and peak acceleration increments into which the hazard is subdivided, $\Delta a_{\max,i}, m_j$ = incremental mean annual rate of non-exceedance for intensity measure $a_{max,i}$ and magnitude m_j. It is important to note that the mean annual rate of <u>non-exceedance</u> is used because non-exceedance of a particular factor of safety (e.g., when $FS_L < 1$) is the undesired condition for liquefaction triggering evaluations.

4.3 Seismic Hazard Analysis

Using a number of various attenuation models or ground motion prediction equations (GMPEs), the USGS National Seismic Hazard Mapping Project (NSHMP) provides seismic hazard maps for the United States (Petersen et al. 2008). Combinations of varying magnitudes and distances to known seismic sources, and conditional exceedance probability levels are input into the GMPEs in order to output a ground shaking hazard curve. McGuire (1995) showed that by deaggregation of the ground shaking hazard at a site of interest, it is possible to quantify the relative contribution of each combination of earthquake magnitude and distance to the seismic source (i.e., each *M-R* pair).

The USGS provides an online tool to deaggregate 2008 NSHMP seismic hazard data at http://geohazards.usgs.gov/deaggint/2008/. This online tool will output the relative contribution of each *M-R* pair for a specified return period associated with a ground motion spectral period (e.g., peak ground acceleration, 0.1 sec, or 0.2 sec, etc.) at a particular latitude and longitude. In order to map the liquefaction triggering hazard in Utah County, points spaced every 0.05 degrees

in latitude and longitude across the study area were systematically input in the USGS online deaggregation tool. The online tool was used to output peak ground acceleration (PGA) values at eight different return periods (i.e., 108, 224, 475, 975, 2475, 4975, 9950, and 19900 years) for every grid point. Magnitude distributions for each of the eight return periods for every grid point were then computed by summing the contributions of each distance and conditional probability exceedance levels according to magnitude. As an example, Fig. 4.4 presents distributions binned in increments of 0.2 of magnitude for four of the eight return periods at one grid point in Utah County. As expected, the lower magnitude earthquakes (i.e., M = 4.6 to 6) contribute more frequently to the seismic hazard at the lower return period of 475 years as compared to the larger return periods ≥ 975 years. In general, earthquakes between M = 6.6 to 7.6 contribute the most to the seismic hazard at all four return periods in the figure. Interestingly, M = 6.8 is the most common (i.e., the modal magnitude). According to the deaggregation reports, the Utah segment of the Wasatch Fault Zone is capable of generating M ≥ 6.6 earthquakes which generate significant ground accelerations. Because this segment is also close to the study area, it is the main contributor to the seismic hazard.

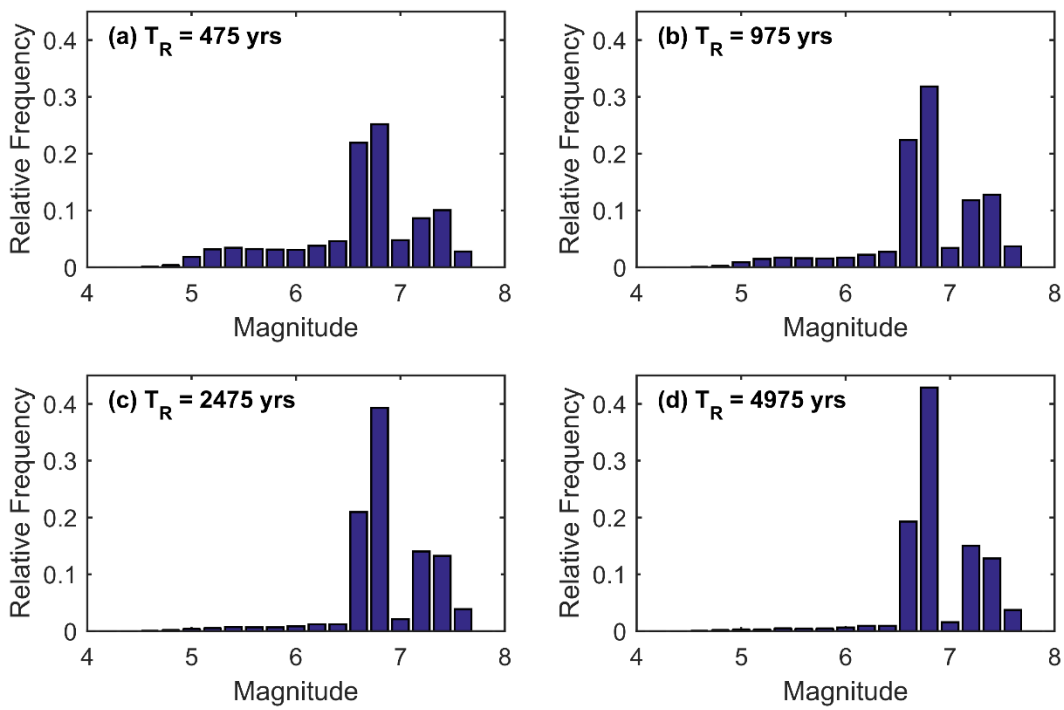

Fig. 4.4. Example distributions of magnitude contributing to a_{max} (site class D soil) for different return periods in a location in Utah County: (a) 475 years, (b) 975 years, (c) 2475 years, and (d) 4975 years.

The PGA hazard curve values output by the USGS online tool in Utah do not account for soft soil effects; rather, they are considered ground accelerations for sites on bedrock. The study area is a relatively deep intermountain basin filled with soft soil that will likely amplify or deamplify the ground accelerations depending on the nature of the strong motion and the characteristics of the soil profile. Thus, a_{max} (i.e., the peak ground acceleration at the ground surface) is found by multiplying PGA by a soil amplification factor, f_a (i.e., $a_{\max} = PGA \cdot f_a$). Unfortunately, f_a also has considerable uncertainty which must be modeled when performing fully probabilistic liquefaction triggering analyses.

Stewart et al. (2003) analyzed numerous time history records and quantified the observed uncertainty in site response based on soil site classification. According to Stewart et al., the natural logarithm of median amplification factor for a given soil column can be represented as a power function as:

$$\ln\left(f_a\right) = a + b\ln\left(PGA\right) \tag{4.3}$$

For the soil at a site classified as Site Class D per the National Earthquake Hazard Reduction Program (NEHRP), $a = 0.08$, $b = -0.07$, and $\sigma_{\ln f_a} = 0.57$. For NEHRP Site Class E, $a = -0.60$, $b = -0.50$, and $\sigma_{\ln f_a} = 0.46$.

To account for uncertainty in site response in the development of input ground motions for liquefaction hazard mapping, the uncertainty defined by Stewart et al. (2003) can be incorporated in to the development of seismic hazard curves for the analysis. In other words, hazard curves in terms of PGA from the USGS can be converted into hazard curves in terms of a_{max}. Assuming a lognormal distribution for the *PGA* and f_a, the mean annual rate of exceeding some assumed peak ground surface acceleration, $a^*_{\max}$ can be computed as:

$$\lambda_{a^*_{\max}} = \int P\left[a_{\max} > a^*_{\max} \mid PGA\right] \cdot \Delta\lambda_{PGA} \tag{4.4}$$

where

$$P\left[a_{\max} > a^*_{\max} \mid PGA,\, f_a\right] = \Phi\left[\frac{\ln PGA + \ln f_a - \ln a^*_{\max}}{\sqrt{\left(\sigma_{\ln PGA}\right)^2 + \left(\sigma_{\ln f_a}\right)^2}}\right] \tag{4.5}$$

and $\Delta\lambda_{PGA}$ is the incremental mean annual rate of exceedance for *PGA* (obtained from the probabilistic seismic hazard analysis for bedrock); $\sigma_{\ln PGA}$ is the natural lognormal standard deviation for the *PGA* (obtained from the ground motion prediction equation(s)); and $\sigma_{\ln f_a}$ is the natural lognormal standard deviation for the soil amplification function.

By combining Equation (4.3) with Equation (4.5), the conditional probability term in Equation (4.4) can be re-written as:

$$P\left[a_{\max} > a^*_{\max} \mid PGA\right] = \Phi\left[\frac{a + (b+1)\ln PGA - \ln a^*_{\max}}{\sqrt{(b+1)^2\left(\sigma_{\ln PGA}\right)^2 + \left(\sigma_{\ln f_a}\right)^2}}\right] \tag{4.6}$$

where a, b, and $\sigma_{\ln f_a}$ depend upon the specified NEHRP site class. Additionally, $\sigma_{\ln PGA}$ can typically be neglected (i.e., $\sigma_{\ln PGA} = 0$) because uncertainty in the estimation of the *PGA* was already accounted for in the probabilistic seismic hazard analysis.

For all aforementioned grid points spaced every 0.05 degrees in latitude and longitude across the study area, Equations (4.4) and (4.6) were applied to convert the set of PGA hazard curves deaggregated on the basis of magnitude (in increments of M = 0.2) to a set of a_{max} hazard curves for <u>both</u> NEHRP Site Class D and E using the Stewart et al. (2003) characterization of uncertainty for site response. Thus, a set of hazard curves for both site classes were computed for each grid point, enabling later selection of the appropriate set of curves based on the soil site class during the liquefaction triggering mapping process as discussed later in this chapter. Examples of the resulting total and incremental $a_{\max}$ hazard curves at a grid point for both the Site Class D and

E assumption are presented in Fig. 4.5. The sum of the hazard curves deaggregated on the basis of magnitude equals the total hazard curve. The hazard curves depicted in Fig. 4.5 are for the same grid point as was used to develop the histograms shown in Fig. 4.4. As expected, the modal magnitude of 6.6 at this grid point is shown in Fig. 4.5 as the hazard curve with the greatest mean annual rate of exceedance per increment of a_{max}.

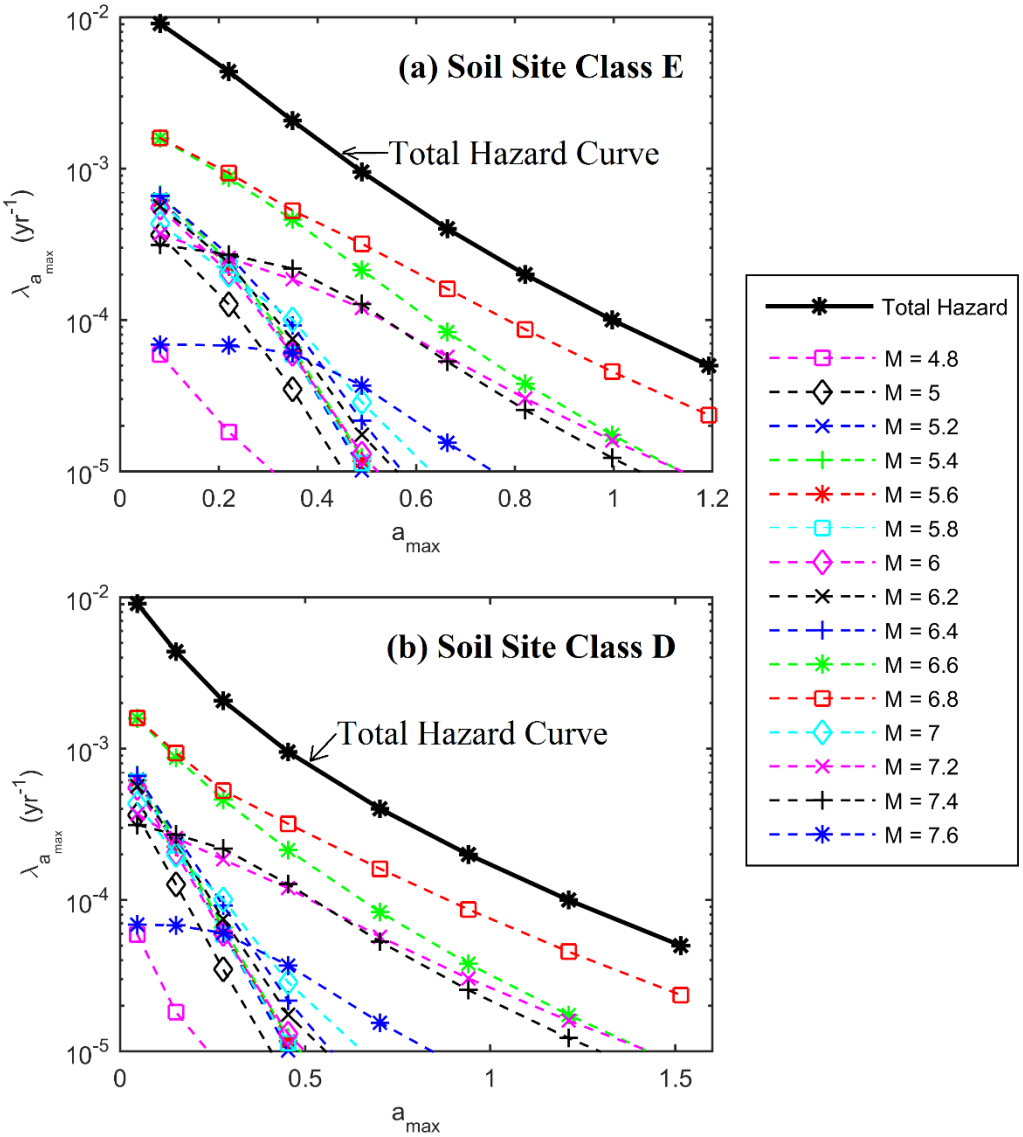

Fig. 4.5. Example a_{max} hazard curves deaggregated on the basis of magnitude for (a) Site Class E soil and (b) Site Class D soil in Utah County. The total hazard curve is equal to the sum of hazard curves for all magnitudes.

The sets of a_{max} hazard curves every 0.05 degrees in latitude and longitude were next bilinearly interpolated to produce a_{max} hazard curves deaggregated on the basis of magnitude and for Site Class D and E soil every 30 m in the study area. As discussed later in this chapter, this interpolation enabled future liquefaction hazard mapping efforts where the factor of safety against liquefaction triggering was computed every 30 m in the study area.

4.4 Probabilistic Liquefaction Triggering Mapping Procedure

By inserting a probabilistic liquefaction triggering model in the framework listed in Eq. 4.2, solving the equation accounts for the uncertainty in the triggering model as well as in the seismic hazard. However, when mapping a regional area, significant uncertainty remains in the subsurface characterization. As a result, Matlab scripts were written to develop fully probabilistic liquefaction triggering maps which model uncertainties in the subsurface characterization, seismic hazard, and empirical triggering model using numerous Monte Carlo simulations. In order to perform a Monte Carlo simulation, a probability distribution must first be developed for each variable that has uncertainty. Then, the variables are randomly sampled from this probability distribution and input into the model. Repeating the random sampling and performing the calculations over and over produces a distribution of outcomes. In this case, a distribution of FS_L values were output at each pixel of the map. The FS_L distributions at each pixel were converted into FS_L-hazard curves, eventually enabling the development of fully probabilistic FS_L hazard maps. The remainder of this chapter provides a discussion on each step of the mapping workflow and Monte Carlo simulations, as illustrated in Fig. 4.6.

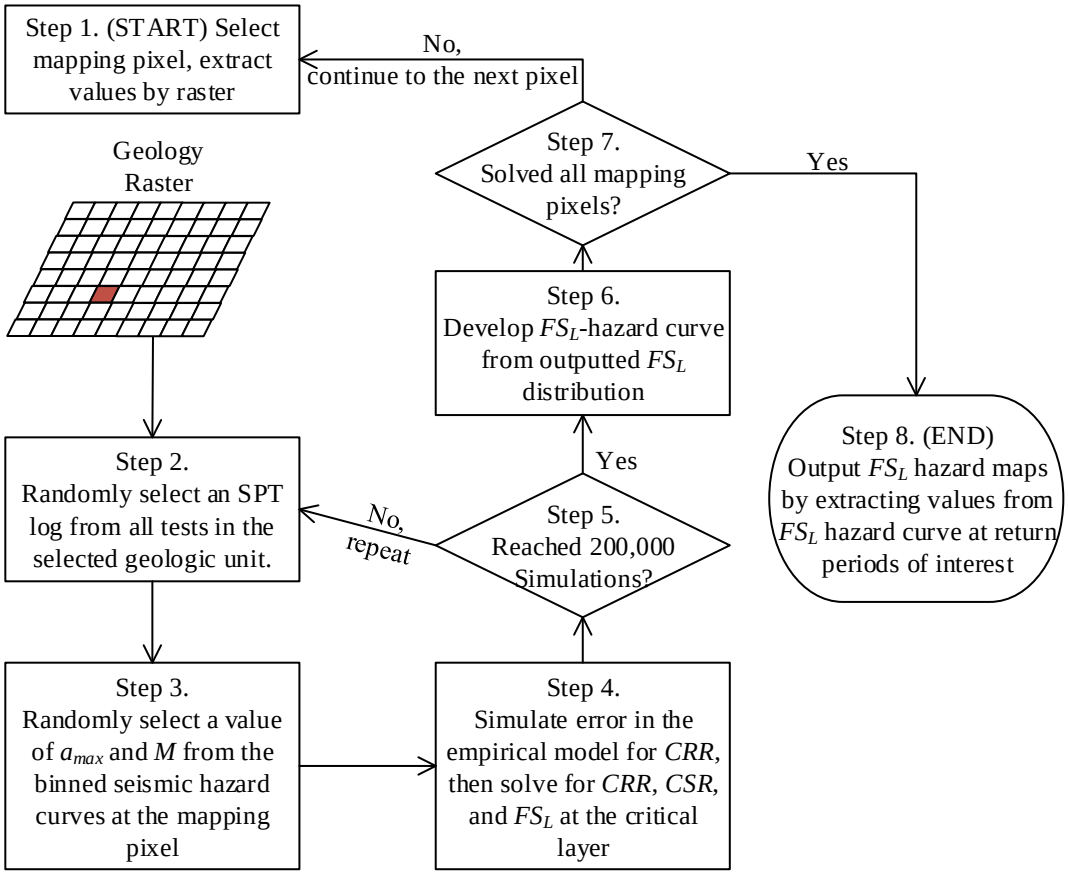

Fig. 4.6. Proposed workflow for mapping the factor of safety against liquefaction triggering (FS_L) hazard for a county

4.4.1. Step 1: Extract Raster Data at a Map Pixel

The authors decided to produce 30-meter horizontal resolution liquefaction triggering hazard maps for the study area in Utah County. A 30-meter resolution map seemed like a reasonable, yet very high-resolution value. In addition, 30-meter resolution seemed appropriate for the subsequent hazard mapping of liquefaction-induced lateral spread displacement, as discussed in the next chapter of this report. Thus, all hazard maps produced in this report have a consistent, horizontal spatial resolution of 30 m.

Following the proposed workflow in Fig. 4.6, the liquefaction triggering hazard was evaluated for each individual 30-meter by 30-meter pixel on the raster map of the study area. The

process was repeated for each pixel, and the results at each pixel were then combined to produce the final hazard maps as raster images.

The hazard mapping procedures proposed in this report rely upon surficial geologic base maps. As explained in Chapter 2, the geology and depositional environment are crucial factors in the susceptibility of a site to liquefaction. Accordingly, the first step of the mapping workflow was to extract the surficial geologic raster value at the location of the selected pixel. For Utah County, these raster values range from 1 – 14, corresponding to the 14 major geologic units defined in Table 3.1.

4.4.2. Step 2: Begin Monte Carlo Simulations, Select an SPT log

Characterizing the subsurface conditions of a widespread geologic unit is challenging, particularly when only using available data instead of planning a geotechnical testing campaign and collecting more data by performing additional drilling, soil sampling, and laboratory testing. Accordingly, the subsurface conditions have considerable uncertainty. In order to model this uncertainty in Utah County, the authors decided to perform numerous Monte Carlo simulations after making three major assumptions: (1) the 14 geologic units listed in Table 3.1 were classified appropriately such that the soil properties within each unit are relatively similar; (2) each SPT investigation provided geotechnical variables at the critical layer (e.g., $(N_1)_{60cs}$, σ'_v, etc.) that can be considered independent, random variables within the geologic unit where the test was conducted; and (3) the sample size of SPT investigations (as listed in Table 3.1) was adequate to approximate the distribution of geotechnical variables in each of the major geologic units. These assumptions had to be made in order to develop distributions of geotechnical variables for each geologic unit and complete the mapping process. Over time, the authors recommend that the

geotechnical database is updated to include additional SPT and CPT investigations collected since the publication of the maps. By expanding the geotechnical database, the distribution of geotechnical variables values for each geologic unit can be refined. Further, by expanding the database, one may find that some of the geologic units should be divided in order to accommodate for localized correlations, major changes in soil layering or groundwater conditions, or other anomalies of soil properties within each mapped geologic unit.

As discussed earlier, 300 Monte Carlo simulations were previously performed at each SPT that reached a minimum drilling depth of 20 ft. in order model uncertainties in the soil weights, stress profiles, and corrections to raw SPT blow count values. This resulted in 300 *solutions* for the total and effective stress profile, and values of $(N_1)_{60,}$ and $(N_1)_{60cs}$ for each layer at the site. In other words, a distribution of total and effective stresses, $(N_1)_{60,}$ and $(N_1)_{60cs}$ with depth were computed at each SPT. In addition, a distribution of $T_{15,cs}$ values for each SPT investigation were computed and were later used for the lateral spread hazard mapping (see Chapter 5). All *solutions* for all of the SPTs were then pooled together according to the major geologic unit in which the test was conducted.

To perform the second step of the mapping process, a new round of Monte Carlo simulations was initiated at the mapping pixel. To start the simulation, one of the 300 *solutions* for one SPT in the geologic unit of the mapping pixel was randomly selected.

4.4.3. Step 3: Input a_{max} and *M*

Continuing with the single Monte Carlo simulation, the next step was to select and input a value for a_{max} and M from the probabilistic seismic hazard analysis (PSHA). This was done by randomly selecting a value for both variables using the a_{max} hazard curves deaggregated on the

basis of magnitude. As discussed earlier, these sets of hazard curves were computed every 30 m in the study area for both Site Class D and E soil profiles (e.g., see Fig. 4.5). Thus, sets of seismic hazard curves for both site classes were available at every mapping pixel in the study area.

In order to choose the appropriate set of hazard curves and model uncertainty in the soil site response, the weighted average for $(N_1)_{60}$ (i.e., $\overline{N}$) was first computed for the upper 30 m of soil profile using the selected SPT from the previous mapping step and following recommended NEHRP provisions (FEMA 2009). NEHRP defines a site with $\overline{N} < 15$ as a soft soil profile (Site Class E), and a site with $15 \leq \overline{N} \leq 50$ as a stiff soil profile (Site Class D). Accordingly, if $\overline{N}$ was found to be less than 15 for the simulation, then the a_{max} hazard curves for Site Class E soils at the mapping pixel were chosen. If $\overline{N}$ was found to be between 15 and 50, then a_{max} hazard curves for Site Class D soils at the mapping pixel were chosen.

Next, the chosen set of hazard curves were converted into units of return period so that the curves could be extended to a point at the origin, or (0,0). Then, linear interpolation along the total hazard curve for a_{max} as well as for each of the hazard curves deaggregated on the basis of magnitude was applied at increments of 0.1 of the logarithm of the return period, producing numerous points along the curves. The non-exceedance probability for each of the points along the total hazard curve for a_{max} was then computed using a Poisson model, and the results were binned into a probability distribution function (PDF) for binned values for a_{max}. Using this PDF, a value for a_{max} was then randomly selected in order to continue with the Monte Carlo simulation.

Since the total hazard curve for a_{max} is also the sum of all of the hazard curves deaggregated on the basis of magnitude, Λ for the selected a_{max} value of each deaggregated hazard curve on the basis of magnitude was divided by Λ for the selected a_{max} value from the total hazard curve. This yielded a PDF of M, or in other words, the contribution for binned earthquake magnitudes

corresponding with a_{max}. Using this PDF, a value for M was then randomly selected and input into the Monte Carlo simulation.

4.4.4. Step 4: Solve for CSR, CRR and FS_L

The final step in the Monte Carlo simulation was to solve for *CSR*, *CRR*, and ultimately FS_L for every layer of soil susceptible to liquefaction using data from the selected SPT solution. The selected values for a_{max} and M from the previous step as well as values for the depth (z) and $(N_1)_{60cs}$ for each layer from the SPT were input into Eqs. 2.8 – 2.14 to find *MSF* and K_σ. All of these values were then input into Eq. 2.2 to find *CSR* for each layer of soil susceptible to liquefaction.

To find *CRR* for the same layers, it was necessary to model the uncertainty in the SPT liquefaction triggering correlation, $\varepsilon_{\ln(R)}$. A value for $\varepsilon_{\ln(R)}$ can be simulated using the normally distributed random number generator function in Matlab, *randn*. Eq. 2.3 was rewritten to the following form:

$$\ln CRR = \frac{(N_1)_{60cs}}{14.1} + \left[\frac{(N_1)_{60cs}}{126}\right]^2 - \left[\frac{(N_1)_{60cs}}{23.6}\right]^3 + \left[\frac{(N_1)_{60cs}}{25.4}\right]^4 - 2.67 + \sigma_{\ln CRR} \cdot randn(1) \qquad (4.7)$$

where the sum of the first five terms on the right side of the equation can be thought of as the mean natural logarithm of *CRR* (i.e., $\overline{\ln CRR}$), σ_{lnCRR} = 0.13, and *randn*(1) is a Matlab function that generates a single random value from the standard normal distribution. Raising Euler's number (e) to the ln*CRR* values produces *CRR* for each of the layers susceptible to liquefaction.

Next, FS_L for each layer was found by simply dividing *CSR* by *CRR* for each layer per Eq. 2.1. Afterwards, for conservatism, the authors considered the layer with the smallest FS_L, or that layer with the smallest factor of safety against liquefaction triggering as the *critical layer*. The FS_L value of the critical layer was then stored as the final output of the Monte Carlo simulation at the mapping pixel.

4.4.5. Step 5: Repeat Steps 2 – 4 for Required Number of Simulations

Numerous simulations were necessary to output FS_L and model the significant uncertainties in the depth and characterization of the critical layer (i.e., $(N1)_{60cs}$), seismic hazard (i.e., M and a_{max}), and liquefaction triggering modeling error (i.e., $\varepsilon_{ln(R)}$). As further discussed below, Steps 2 – 4 were repeated 200,000 times at each mapping pixel, outputting a distribution of possible FS_L values at a mapping pixel.

4.4.6. Step 6: Develop FS_L Hazard Curve

The next step in the mapping procedure was to convert the 200,000 FS_L values at a mapping pixel from the Monte Carlo simulations into a FS_L-hazard curve. To make this conversion, the distribution for FS_L was first converted into an empirical cumulative distribution function (CDF) curve. The annual probability that FS_L does *not* exceed a selected factor of safety value, FS_L^*, of interest (i.e., $P(FS_L < FS_L^*)$ is equal to the CDF value at FS_L^* on this curve. This annual non-exceedance probability is also defined using the Poisson probability model as:

$$P(FS_L < FS_L^*) = 1 - e^{(-\Lambda t)} \tag{4.8}$$

where t = 1 year for an annual probability, and Λ = the mean annual rate of non-exceedance where its inverse (i.e., $1/\Lambda$) = the return period in years.

Table 4.1 lists some typical return periods of interest and their corresponding values of Λ, and the annual non-exceedance probability value (i.e., or CDF value). Intermediate points on the FS_L-hazard curve at a mapping pixel were developed by using the empirical CDF curve and by finding the FS_L^* value at numerous CDF values, such as those listed in Table 4.1. The fourth column of Table 4.1 presents an example set of FS_L^* values for each of the listed CDF values at a mapping pixel in the study area. Plotting Λ versus FS_L^* from Table 4.1, the FS_L-hazard curve for this example set of data can be depicted, as per the example in Fig. 4.7a. (Note the hazard curve was actually computed and plotted using more data points than the example data listed in Table 4.1.)

In order to understand results, it is worth discussing the data presented in Fig. 4.7a and Table 4.1. Liquefaction is expected to occur when $FS_L < 1$. As can be seen, FS_L at this example mapping pixel is much greater than 1 at return periods of less than 475 years. At a return period of 475 years, the resistance of the soil to triggering (*CRR*) is more than double the stress induced by the earthquake shaking (*CSR*). However, for the more extreme hazards with a return period of 1033 years or greater, FS_L is less than 1. The seismic shaking from earthquakes associated with more extreme hazard levels may trigger liquefaction. Another way to understand the results is to consider the CDF values listed in Table 1. The 1033-year return period hazard corresponds with a CDF value equal to 0.1%. This means that only 0.1% of the 200,000 Monte Carlo simulations (i.e., 200 out of 200,000) output FS_L values less than $FS_L^* = 0.9$. In addition, based on the data below, it can be concluded that the return period of liquefaction triggering (i.e., when $FS_L = 1$) at this mapping pixel is approximately 1,000 years.

Numerous simulations ensure that the uncertainties in the mapping process are modeled well, and that the extreme outputs from the models are captured for hazard mapping purposes. As stated earlier, the authors decided to run 200,000 simulations for each mapping pixel. This large number may not have been necessary for mapping the liquefaction triggering hazard; however, it was considered necessary for mapping the lateral spread hazard (see Chapter 5). As a result, the same number of simulations were used for mapping both the liquefaction triggering and lateral spread hazards. Fig. 4.7b presents FS_L-hazard curves at the same mapping pixel after running 10000, 50000, 100000, 200000, 300000, and 400000 simulations. As can be seen, all of the curves look quite similar (especially when N $\geq$ 50,000 simulation) and one could argue that N $\approx$ 50,000 simulations is adequate for modeling the uncertainties in the liquefaction triggering mapping procedure.

Table 4.1. Example distribution of FS_L values at listed return periods

Return Period [$1/\Lambda$] (years)	Mean annual rate of non-exceedance, Λ	CDF, or annual non-exceedance probability [$P(FS_L < FS_L^*)$]	FS_L^*
108	0.01	0.009	> 10
228	0.004	0.0044	> 10
475	0.002	0.0021	2.1
1033	0.001	0.0010	0.9
2475	0.0004	0.00040	0.6
4975	0.0002	0.00020	0.4
9975	0.0001	0.00010	0.3

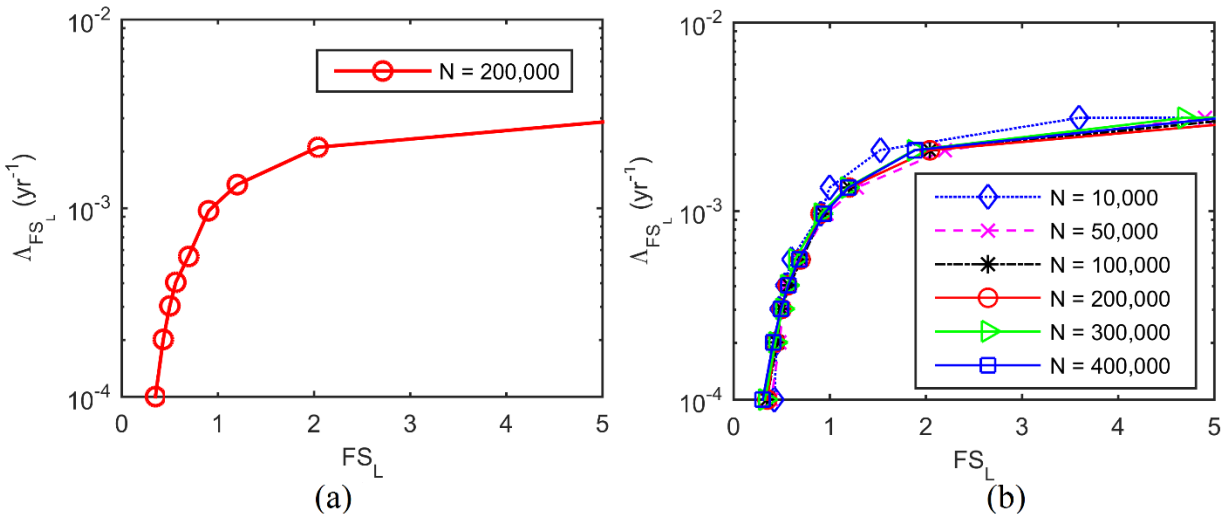

Fig. 4.7. (a) Example FS_L-hazard curve at a mapping pixel after 200,000 Monte Carlo simulations; a set of FS_L -hazard curves at the same mapping pixel after noted numbers of Monte Carlo simulations.

4.4.7. Step 7: Repeat Previous Steps for all Mapping Pixels

The first six steps of the mapping procedure were repeated for every mapping pixel in the study area. Upon completion, a FS_L-hazard curve similar to the one depicted in Fig. 4.7a was generated for every 30-m mapping pixel in the study area in Utah County.

4.4.8. Step 8: Output Maps for Desired Return Periods

The final step was to produce 30-m resolution raster hazard maps at desired return periods. This was done by simply extracting the FS_L value from the FS_L -hazard curve at a desired return period (e.g., 475, 1033, or 2475-year return period) for each mapping pixel, then storing each of them as raster values in an image of the study area. The raster images for return periods of 475, 1033, and 2475 years were then loaded in GIS and added to available spatial data layers from the AGRC (e.g., transportation routes, location of major lakes, etc.) to produce the final hazard maps. Figs. 4.8 through 4.10 present FS_L hazard maps of the study area at return periods of 475, 1033, and 2475 years, respectively.

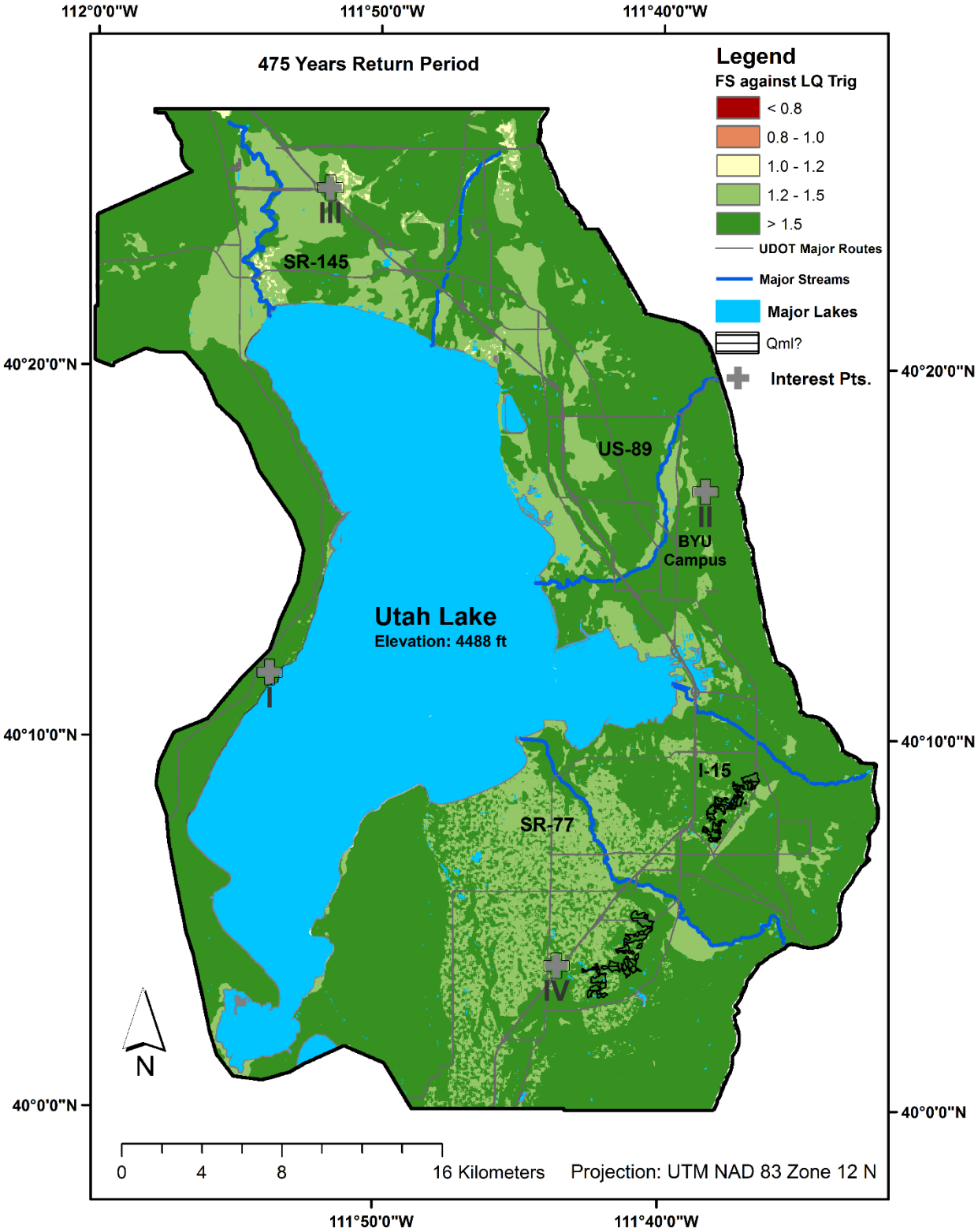

Fig. 4.8. The 475-year return period (10% probability of exceedance in 50 years) liquefaction triggering hazard map, Utah County, Utah.

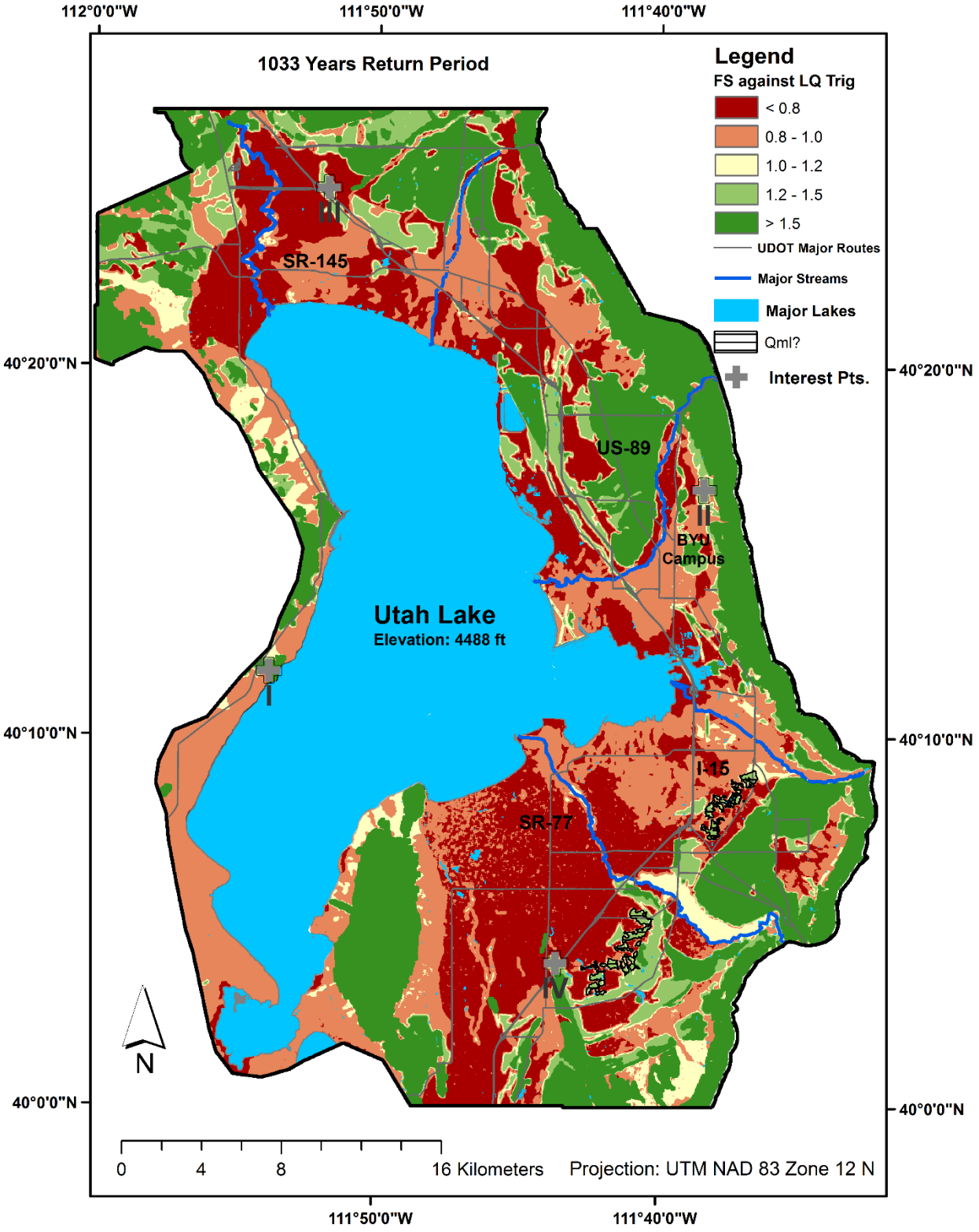

Fig. 4.9. The 1033-year return period liquefaction triggering hazard map, Utah County, Utah.

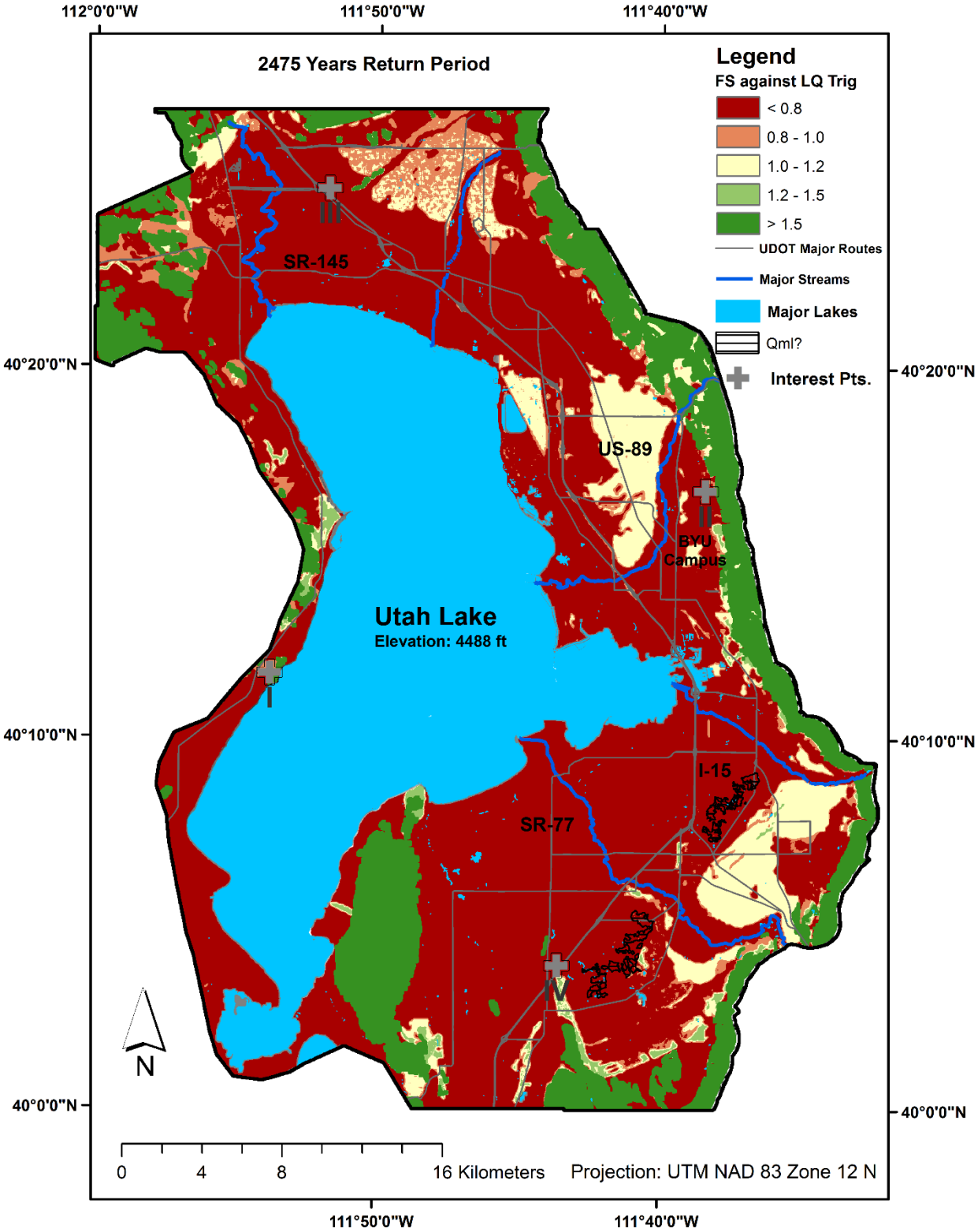

Fig. 4.10. The 2475-year return period (2% probability of exceedance in 50 years) liquefaction triggering hazard map, Utah County, Utah.

4.5 Discussion of the Liquefaction Triggering Hazard Maps for Utah County

Unfortunately, similar to the previous mapping efforts in Utah County (e.g., Anderson et al. 1994), the triggering hazard maps imply widespread liquefaction may occur during a major seismic event in Utah County. However, the figures presented in this report provide an enhanced indication of the likelihood of triggering because the maps are shown in terms of the return period of the hazard. For instance, the 475-year return period hazard map in Fig. 4.8 shows that liquefaction triggering is unlikely. As shown, FS_L is greater than 1 for the entire study area. It appears that the earthquakes associated with this hazard level are insufficient to trigger liquefaction. This finding may be important, as some building codes require engineers to design structures, foundations, and lifelines to withstand a 475-year return period hazard. At this return period, liquefaction appears to be unlikely.

However, for more-critical infrastructure, building codes may require engineers to design for greater hazard levels. In some cases, an engineer may be required to account for a 1033- or 2475-year return period hazard. At the 1033- or 2475-year return period hazard, liquefaction appears to be a significant problem. Per the seismic hazard deaggregation section of this report, the Utah segment of the Wasatch Fault Zone is the main contributor to the seismic hazard, especially at return periods of 1033 years or greater. Because of the proximity to the study area, modeled earthquakes from the Utah segment of the Wasatch Fault Zone are so strong that they generate large *CSR* values which frequently produce values of $FS_L < 1$ in soil layers that are susceptible to liquefaction. Given the widespread triggering hazard at the greater return periods, it is important to next investigate the potential consequences of liquefaction. The following chapter of this report presents a methodology for mapping the lateral spread hazard.

Lastly, it is worth mentioning that the geologic map for Utah County (Fig. 3.1) identifies some small deposits east of the I-15 corridor and southeasterly of Utah Lake which may have underwent lateral spreading during a prehistoric earthquake. These deposits were labeled as "Qml? Lateral-spread deposits?" on the Constenius et al. (2011) map. Harty and Lowe (2003) named these deposits the Beer Creek and Springville/Spanish Fork features. Unfortunately, none of the available investigations in the geotechnical database were within these deposits. Given that they may have underwent lateral spreading in the past, and because of a lack of geotechnical data in these deposits, these areas were hatched in hazard maps in Figs. 4.8 through 4.10. Further research is needed to determine the liquefaction triggering and lateral spread hazard for the *Qml?* deposits.

5. Lateral Spread Mapping

The maps presented in the previous chapter of this report are useful for identifying the likelihood of liquefaction triggering; however, these maps do not provide any information on the consequences of the triggering. In some areas, the maps in Chapter 4 might have only identified a thin or relatively deep layer of soil which may trigger during a major earthquake, resulting in minor or no ground failures. In other areas, thick and continuous layers may trigger resulting in ground surface settlements or lateral spreading. Simply stated, the triggering maps do not illustrate the severity or the type of possible ground failures induced by liquefaction.

Thus, it is important to not only map the triggering of liquefaction, but also map the consequences of such triggering. As discussed in Chapter 2, the most pervasive type of liquefaction-induced ground failure is lateral spreading. Hence, mapping and identifying areas prone to severe lateral spreading, or areas where the largest horizontal displacement due to lateral spreading may occur, is particularly helpful for identifying the most-critical locations for liquefaction hazard mitigation. The following chapter presents a procedure for the probabilistic estimation and mapping of liquefaction-induced lateral spread displacements. The procedure is then implemented to map the lateral spread hazard in the study area for Utah County.

5.1 Probabilistic Model for Displacement Prediction

Franke and Kramer (2013) developed a procedure that incorporates the Youd et al. (2002) empirical model for estimating lateral spread displacements into a probabilistic framework that considers the uncertainty in the predicted displacement given the magnitude, *M*, and source-to-site

distance, R. This procedure can be readily modified to use the Gillins and Bartlett (2013) empirical model rather than the Youd et al. (2002) model.

If one were to ignore the error, ε, in Eq. 2.15, then the equation will produce the mean value of $logD_H$ (i.e., $\overline{logD_H}$). As discussed in Chapter 2, the standard deviation of the model, σ_{logDH} = 0.2232. Similar to the Youd et al. (2002), Gillins and Bartlett (2013) did not assign error contributions to the various sources of case history data for the regression analysis, such as for the seismic loading, site geometry, SPT resistance, displacement measurement, etc. Thus, σ_{logDH} is a measurement of the total model uncertainty. Accordingly, the probability of exceeding some non-zero lateral spread displacement, d, can be computed as:

$$P(D_H > d) = 1 - \Phi\left(\frac{\log d - \overline{\log D_H}}{0.2232}\right) \tag{5.1}$$

where Φ is the standard normal cumulative distribution.

5.2 Performance-Based Lateral Spread Model

The probabilistic form of the Gillins and Bartlett (2013) model can be used as a basis for a fully probabilistic, performance-based model for mapping lateral spreading displacement. Again, following a similar step as in Franke and Kramer (2013), the various components of Eq. 2.15 can be rewritten in a simple form as:

$$\log D_H = L + G + \varepsilon \tag{5.2}$$

where L, G, and ε represent quantities describing the apparent loading, site geometry, and model uncertainty, or:

$$L = b_1 M + b_2 \log R^* + b_3 R \tag{5.3}$$

$$G = b_0 + b_4 \log W + b_5 \log S + b_6 \log T_{15,cs} \tag{5.4}$$

As discussed in Chapter 4, the Pacific Earthquake Engineering Research Center (PEER) provides a modular framework consisting of individual components that may be combined to evaluate a specific system performance. The PEER framework states that the mean annual rate of exceeding a given *EDP* level, *edp*, given a particular intensity measure ($IM = im_i$) can be computed by:

$$\lambda_{edp} = \sum_{i=1}^{N_{IM}} P(EDP > edp \mid IM = im_i) \Delta\lambda_{im_i} \tag{5.5}$$

where $\Delta\lambda_{imi}$ is the increment of intensity measure hazard, and $P(EDP > edp \mid IM = im_i)$ is the probabilistic response model that relates *EDP* to *IM*.

Inserting Eqs. 5.1 and 5.2 into Eq. 5.5 produces a performance-based model or the mean annual rate of lateral spread displacement exceeding some non-zero lateral spread value, conditioned on the site geometry parameter, *G*.

$$\lambda_{D_H|\mathrm{G}} = \sum_{i=1}^{N_L} P(D_H > d \mid \mathrm{G}, \mathrm{L}_i)\Delta\lambda_{L_i} \tag{5.6}$$

where $\Delta\lambda_{Li}$ is the increment of apparent loading hazard, and N_L is the number of loading parameter increments required to span the range of possible L values.

5.3 Probabilistic Lateral Spreading Mapping Procedure

Eq. 5.6 provides a model for the proposed lateral spread mapping procedure given a particular value for G. However, in the case of mapping the lateral spread hazard for a large county, G has uncertainty due to uncertainty in $T_{15,cs}$. Instead of solving the summation directly, the lateral spread hazard maps in Utah County were developed by performing numerous Monte Carlo simulations using custom Matlab scripts. Thus, the procedure was quite similar to the procedure for mapping the liquefaction triggering hazard. The remainder of this chapter provides a discussion on each step of the mapping workflow and Monte Carlo simulations, as illustrated in Fig. 5.1.

5.3.1. Step 1: Extract Raster Data at a Map Pixel

Similar to the liquefaction triggering maps, it was necessary to initially decide which spatial resolution was most appropriate for mapping the lateral spread hazard. The Gillins and Bartlett (2013) empirical model was regressed from numerous case histories of lateral spreading. In general, the ground slopes for each of these case histories were measured as the average slope across a length of around 15 – 50 m (Bartlett and Youd 1992). Hence, a 30-meter resolution map seems like a reasonable, yet very high-resolution value for lateral spread hazard mapping.

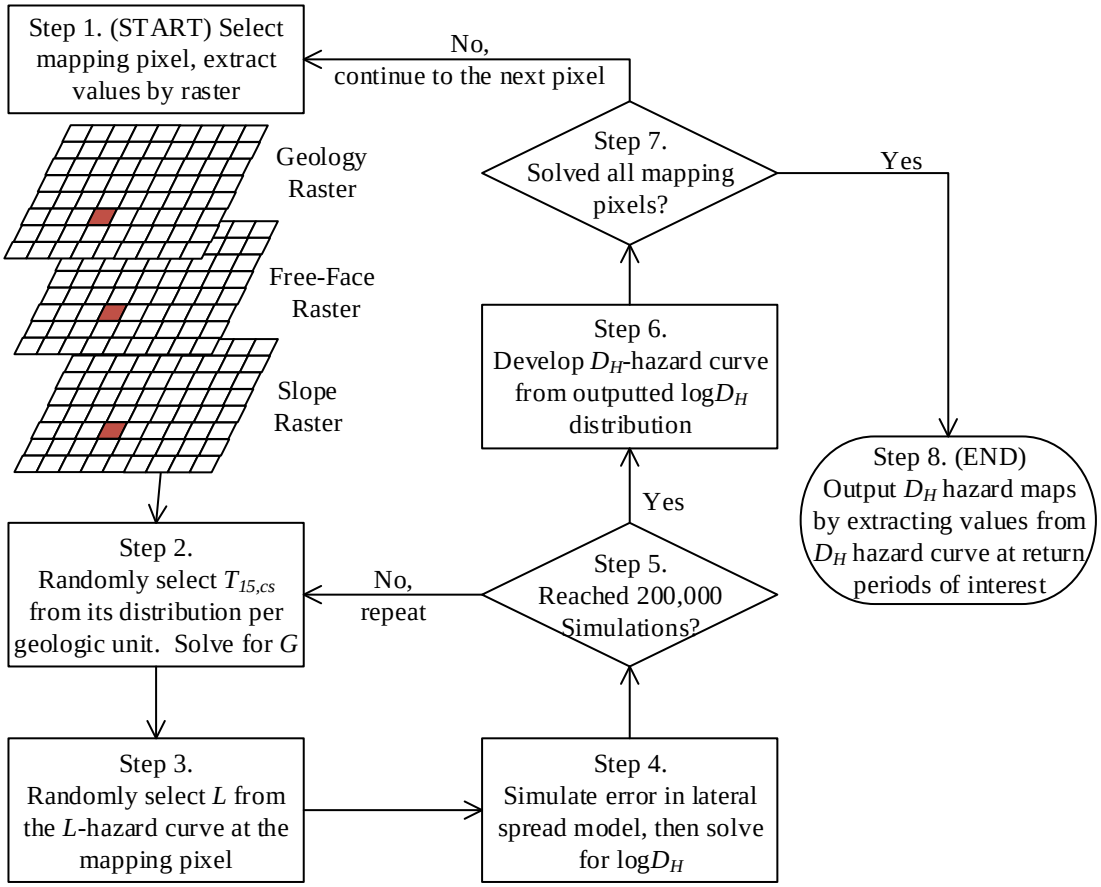

Fig. 5.1. Proposed workflow for mapping the lateral spread hazard for a county

Following the proposed mapping workflow, the lateral spread hazard was evaluated for each individual 30-meter by 30-meter pixel. The process was then repeated for each pixel, and the results at each pixel were then combined to produce the final hazard maps at a 30-m horizontal resolution.

The first step of the mapping workflow was to extract the surficial geologic raster value at the location of the selected pixel using GIS tools. In addition, the slope and free-face raster values were extracted from the raster maps for the study area to produce values of S and W, respectively, for input in Eq. 5.4. The slope and free-face ratio raster maps were generated for Utah County following steps in Bartlett and Gillins (2013) and Gillins (2014) using the aerial lidar data as the

source DEM, described in Chapter 2. The uncertainty in the aerial lidar DEM was considered negligible as compared to the uncertainty in probabilistic seismic hazard analysis, subsurface characterization, and lateral spread empirical model. Therefore, uncertainties in the estimation of *S* and *W* were not modeled when mapping Utah County.

5.3.2. Step 2: Begin Monte Carlo Simulations, Input $T_{15,cs}$

Eq. 5.6 has one geotechnical variable, $T_{15,cs}$. Unless a detailed geotechnical investigation directed at analyzing the liquefaction hazard was conducted at the mapping pixel, $T_{15,cs}$ typically has considerable uncertainty due to challenges in characterizing the subsurface and the limited number of available geotechnical investigations. Thus, 3 major assumptions were made in order to complete the mapping process, as listed in Chapter 4. Chapter 4 also explained that 300 Monte Carlo simulations were performed at each SPT reaching a minimum depth of 20 ft. in order model uncertainties in the soil unit weights, stress profiles, and corrections to raw SPT blow counts. These 300 simulations computed a distribution of $(N_1)_{60}$ values with depth at each borehole, which also produced a distribution of $T_{15,cs}$ values for each SPT investigation.

Values of $T_{15,cs}$ for each of the 300 simulations were computed per definitions given in Chapter 2. A value of $T_{15,cs}$ was computed by first finding the thickness of those soils at the site which were both considered susceptible to liquefaction (i.e., only saturated, cohesionless soils) *and* had values of $(N_1)_{60} \leq 15$. Soil above the groundwater table or described as *clay, cobbles, limestone,* or *organic material* were screened out from the calculation of $T_{15,cs}$.

Afterwards, the distributions of $T_{15,cs}$ at the boreholes were pooled together according to geologic unit, developing a distribution of $T_{15,cs}$ for each of the 14 major geologic units. Fig. 5.2 illustrates hazard curves developed from the distributions of $T_{15,cs}$ for each of the major geologic units in the study area. This plot provides an interesting way to compare which units are more or

less likely to have thick layers of soil which may undergo lateral spreading during a major earthquake. Holding all other variables in Eq. 5.2 constant, sites with relatively larger values of $T_{15,cs}$ will displace horizontally greater distances during lateral spreading. SPT borehole logs in the lacustrine units (e.g., lacustrine sand, fine-grained lacustrine) tended to show larger $T_{15,cs}$ values, whereas the older alluvial fans and alluvial fans and terraces tended to have smaller $T_{15,cs}$ values.

To perform the second step of the mapping process, a new round of Monte Carlo simulations was initiated at the mapping pixel. For a single simulation, a value for $T_{15,cs}$ was randomly selected from the distribution of $T_{15,cs}$ values for the geologic unit of the mapping pixel. Given W and S from the previous step, and the randomly selected value of $T_{15,cs}$, Eq. 5.4 was then solved. The regression coefficients for Eq. 5.4 vary depending on the topography at the point of interest. For conservatism, Eq. 5.4 was solved twice—once for free-face conditions and once for ground-slope conditions. Then, the maximum value was used for G in the simulation.

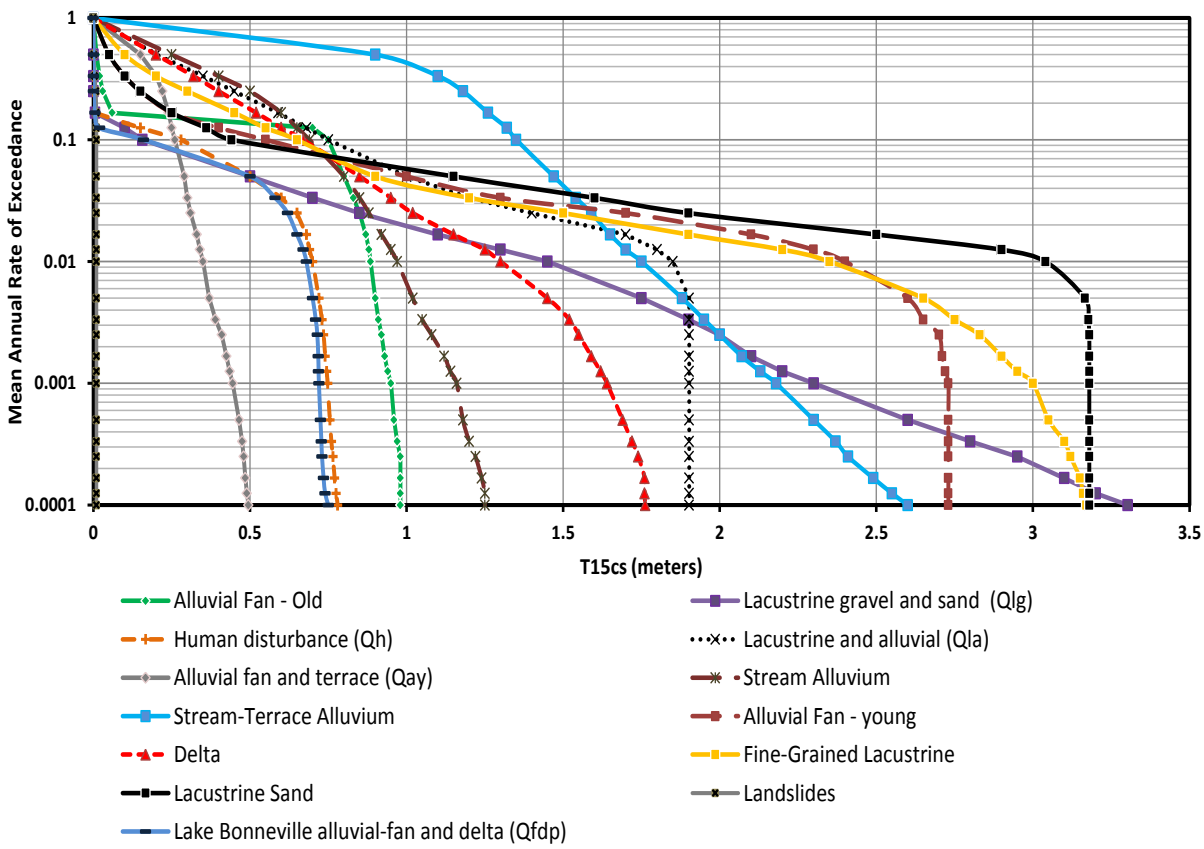

Fig. 5.2 – Hazard curves of $T_{15,cs}$ for each geologic unit

5.3.3. Step 3: Input Apparent Loading Value, L

Continuing with the single Monte Carlo simulation, the next step was to select and input an apparent loading value, *L*, in order to eventually solve Eq. 5.2. Of course, *L* has significant uncertainty, and in order to output fully probabilistic lateral spread hazard maps, *L* must be modeled by performing a probabilistic seismic hazard analysis (PSHA).

To perform the PSHA, EZ-FRISK software (version 7.62) was used to output hazard curves for *L* at grid points evenly spaced every 0.05 degrees in latitude and longitude for the study area. Franke (2005) outlined a procedure for programming EZ-FRISK to output an *L*-hazard curve. First, the attenuation relationship for *L* was entered in the program by using the *Attenuation Table* feature of the program. Values of *L* were entered into the Attenuation Table by solving Eq. 5.3 at

values of *M* from 4.6 to 8.4 (in increments of 0.2), and values of *R* of 1, 5, 10, 15, 20, 25, 30, 40, 50, 60, 70, 80, 90, 100, 125, 150, 175, 200, 250, and 300 km. EZ-FRISK does not allow values of zero for the standard deviation of *L*, so a very small value of 0.0001 was used. Since *L* is not a measured ground motion parameter and was defined in this report, a very small standard deviation is a valid assumption (Franke 2005). EZ-FRISK was set to use the USGS 2008 faults, areas, and background sources to perform the PSHAs. All USGS seismic sources within 500 km of each grid point were included in the PSHAs, and hazard values for *L* were output for return periods of 100, 275, 475, 1000, 2500, 5000, and 10000 years. Fig. 5.3 presents *L*-hazard curves at four grid points in the study area. The location of these four grid points is shown in Fig. 5.4.

Afterwards, 30-m resolution raster maps of *L* for the above return periods were generated by bilinear interpolation of the *L*-hazard curves computed at the evenly spaced grid points. Fig. 5.4 illustrates these raster maps for *L* at return periods of 1000, 2500, and 5000 years. These *L-hazard maps* show the variation in the hazard for *L* across the study area.

To perform the third step of the mapping process and continue with the Monte Carlo simulation, raster values for *L* were first extracted from each of the seven *L-hazard maps* at the mapping pixel. This produced seven intermediate points on an *L*-hazard curve at the mapping pixel (similar to the points on the curves depicted in Fig. 5.3). The points were then converted to units of return period so that an eighth intermediate point at (0,0) could be added. Then, a linear interpolation (in increments of 0.1) between each of the eight intermediate points was applied to the logarithm of the return period of the points, enabling production of numerous points along the *L*-hazard curve at the mapping pixel. The exceedance probability for each of the points on the hazard curve were then computed using a Poisson model, and the results were binned into a

probability distribution function (PDF) for binned values of *L*. Afterwards, a value for *L* was randomly selected from the PDF for *L*.

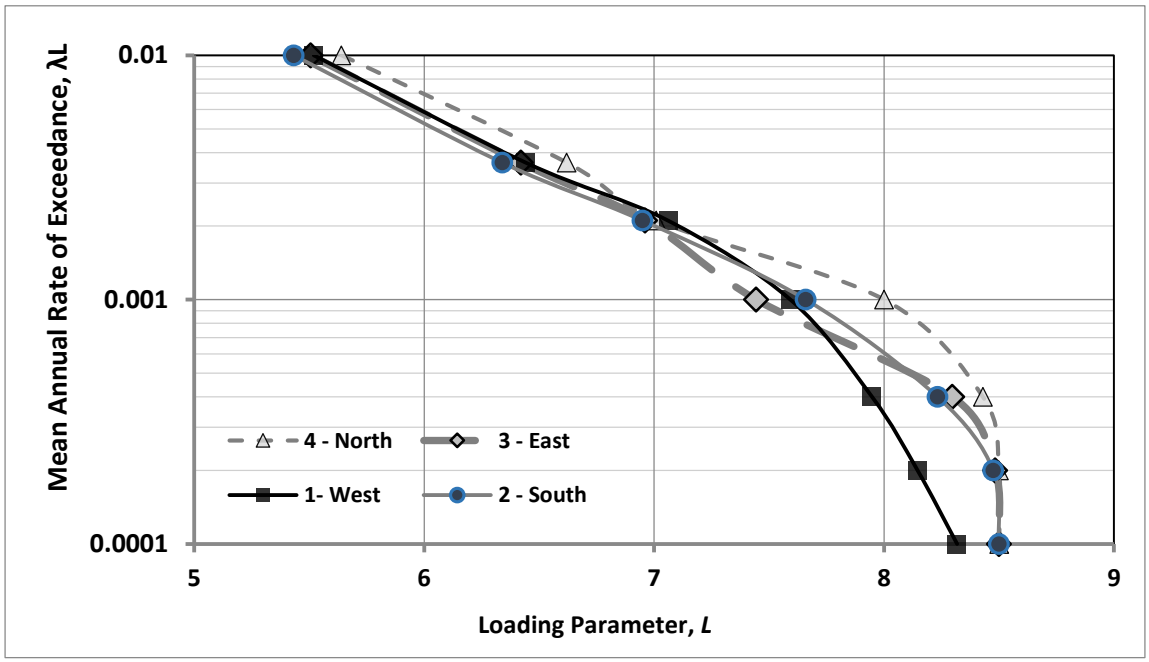

Fig. 5.3. Apparent loading parameter hazard curves for four discrete locations in Utah County; the locations are identified in Fig. 5.4.

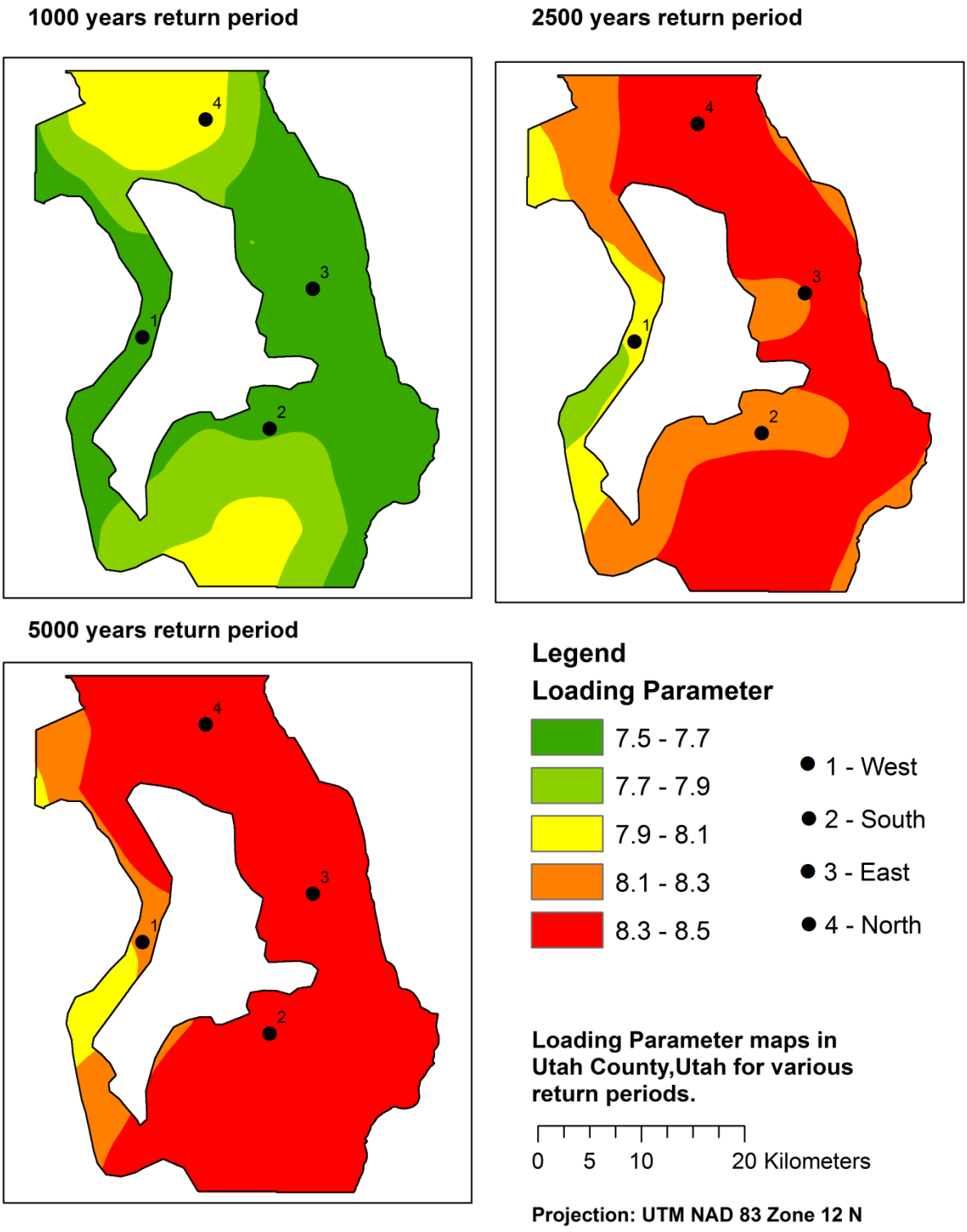

Fig. 5.4. Apparent loading parameter hazard maps for a 1,000-year, 2,500-year, and 5,000-year return period in Utah County.

5.3.4. Step 4: Compute $logD_H$

The final step in the Monte Carlo simulation was to solve Eq. 5.2. The sum of G from Step 2 and the selected value for L from Step 3 produces the mean value of $logD_H$ (i.e., $\overline{logD_H}$). A value for the error in the lateral spread displacement model, ε, can be simulated using the normally distributed random number generator function in Matlab *randn*. In other words, Eq. 5.2 can be rewritten to the following form:

$$\log D_H = \overline{\log D_H} + \sigma_{\log DH} \cdot randn(1) \tag{5.7}$$

where $\overline{logD_H} = G + L$, $\sigma_{logDH} = 0.2232$ and *randn*(1) is a function that generates a single random value from the standard normal distribution.

Solving Eq. 5.7 produces an estimate of the logarithm to base 10 of the horizontal lateral spread displacement from a single Monte Carlo simulation.

5.3.5. Step 5: Repeat Steps 2 – 4 for Required Number of Simulations

Numerous simulations are necessary to model the uncertainties in the subsurface characterization (i.e., $T_{15,cs}$), seismic hazard (i.e., L), and lateral spread displacement modeling error (i.e., ε). As further discussed below, Steps 2 – 4 were repeated 200,000 times, resulting in a distribution of $logD_H$ values at a mapping pixel. This distribution was then converted into a distribution of D_H values (in meters) at a mapping pixel by raising 10 to the $logD_H$ values.

5.3.6. Step 6: Develop a D_H Hazard Curve

The next step in the mapping procedure was to convert the 200,000 D_H values at a mapping pixel from the Monte Carlo simulations into a D_H-hazard curve. To make this conversion, the distribution for D_H was first converted into an empirical cumulative distribution function (CDF) curve. The annual probability that D_H exceeds a displacement value, d, of interest (i.e., $P(D_H > d)$) is equal to *1 minus the CDF* value at d on this curve. (Note that the CDF is always equal to the non-exceedance probability; therefore, in this case, the CDF equals the probability D_H does not exceed d). The annual exceedance probability is also defined using the Poisson probability model as:

$$P(D_H > d) = 1 - e^{(-\lambda t)} \tag{5.8}$$

where t = 1 year for an annual probability, and λ = the mean annual rate of exceedance where its inverse (i.e., $1/\lambda$) = the return period in years.

Table 5.1 lists some typical return periods of interest and their corresponding values of λ, annual exceedance probability, and CDF. Intermediate points on the D_H-hazard curve at a mapping pixel were developed by using the empirical CDF and finding the D_H value at each of the CDF values listed in Table 5.1. The fifth column of Table 5.1 presents an example set of D_H values for each of the listed CDF values at a mapping pixel in the study area. Plotting λ versus d from Table 5.1, the D_H-hazard curve for this example set of data can be depicted, as shown in Fig. 5.5a.

It is interesting to consider the meaning of the hazard curve depicted in Fig. 5.5a and tabulated in Table 5.1. For a 475-year or 2,475-year return period hazard, the annual exceedance probability equals only 0.2% and 0.04%, respectively. Clearly, for a given year, these extreme

hazard levels are highly unlikely; nonetheless, engineers are concerned with such hazard levels because the extreme events can cause significant damage. Upon further inspection of the example data in Table 5.1, 0.2% (or 400 of the 200,000 simulations) of the data in the D_H distribution at the mapping pixel exceeded a displacement value of 0.01 m, and only 0.04% (or 80 of the 200,000 simulations) exceeded a displacement value of 0.43 m. These lateral spread displacement values of 0.01 m and 0.43 m therefore correspond to the 475-year and 2475-year return period hazards, respectively.

Since the extreme values in the D_H distributions are of greatest interest when mapping the lateral spread hazard, it is important to perform many Monte Carlo simulations. In addition, numerous simulations ensure that the uncertainties in the mapping process are modeled well. As stated earlier, the authors decided to run 200,000 simulations for each mapping pixel. This large number was selected because it produced a D_H-hazard curve that looked similar to a D_H-hazard curve after 300,000 or 400,000 simulations at return periods less than 2475 years, and it did not overburden the computer. For example, Fig. 5.5b presents D_H-hazard curves at the same mapping pixel after running 10000, 50000, 100000, 200000, 300000, and 400000 simulations. The curve for 10000 simulations appears different than the other curves, and the authors conclude after several tests that this number of simulations was inadequate. The curves appear fairly similar when $N \geq 100000$ simulations, especially at return periods less than 2475 years (i.e., $\lambda < 0.0004$).

Table 5.1. Example distribution of D_H values at listed return periods

Return Period [$1/\lambda$] (years)	Mean annual rate of exceedance, λ	Annual Exceedance Probability [$P(D_H > d)$]	CDF [$P(D_H < d)$]	d (meters)
108	0.01	0.009	0.991	0.00
228	0.004	0.0044	0.9956	0.00
475	0.002	0.0021	0.9979	0.01
1033	0.001	0.0010	0.9990	0.06
2475	0.0004	0.00040	0.99960	0.43
4975	0.0002	0.00020	0.99980	1.84
9975	0.0001	0.00010	0.99990	3.45

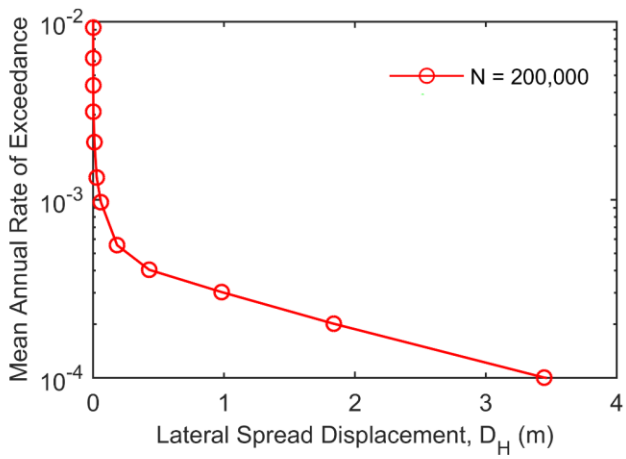

(a)

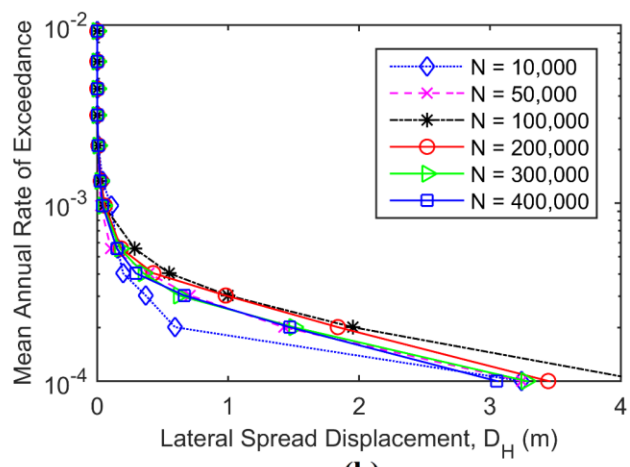

(b)

Fig. 5.5. (a) Example D_H-hazard curve at a mapping pixel after 200,000 Monte Carlo simulations; (b) a set of D_H -hazard curves at the same mapping pixel after various numbers of Monte Carlo simulations.

5.3.7. Step 7 Repeat Previous Steps for All Mapping Pixels

The first six steps of the mapping procedure were repeated for every mapping pixel in the study area. Upon completion, a D_H-hazard curve similar to the one depicted in Fig. 5.5a was generated for every 30-m mapping pixel in the study area in Utah County.

5.3.8. Step 8: Output Maps for Desired Return Periods

The final step was to produce 30-m resolution raster hazard maps at desired return periods. This was done by simply extracting the D_H value from the D_H -hazard curve at a desired return period (e.g., 475, 1,33, or 2475-year return period) for each mapping pixel, then storing each of them as raster values in an image of the study area. Since the D_H -hazard curves were already computed at a resolution of 30-m for the study area, no additional interpolation was necessary. The raster images for return periods of 475, 1033, and 2475 years were loaded in GIS and added to available spatial data layers from the AGRC (e.g., transportation routes, location of major lakes, etc.) to produce the final hazard maps.

Fig. 5.6 and Fig. 5.7 present D_H hazard maps of the study area at return periods of 1,033 and 2,475 years. A 475-year return period hazard map is not presented in this report because the procedure produced negligible D_H values for the entire study area. Note that this finding was consistent with the 475-year return period liquefaction triggering map, where triggering was found to be highly unlikely for the entire study area. The authors conclude that the 475-year return period seismic hazard in Utah County is too small to trigger liquefaction or induce lateral spread displacements.

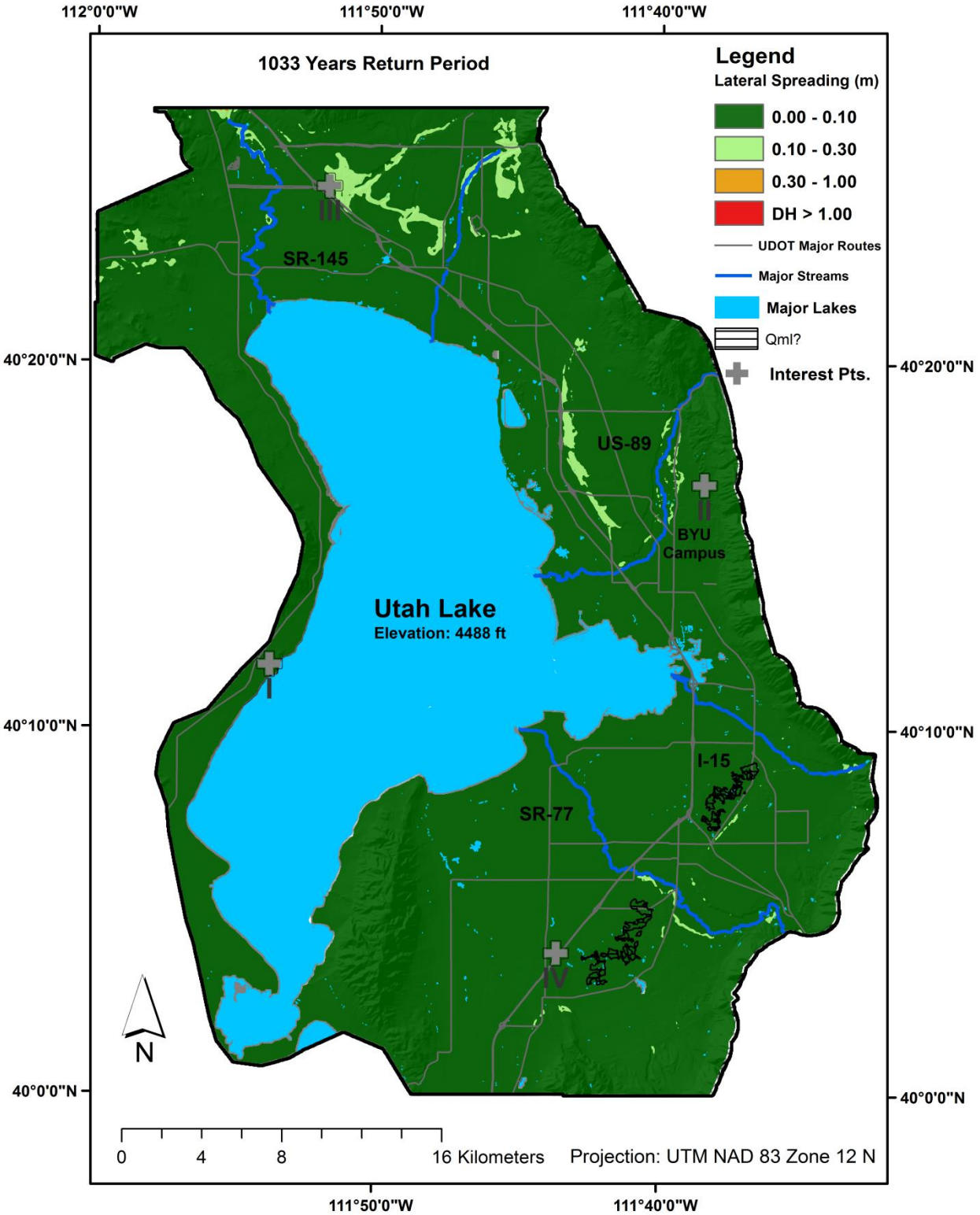

Fig. 5.6. The 1,033-year return period lateral spread hazard map, Utah County, Utah.

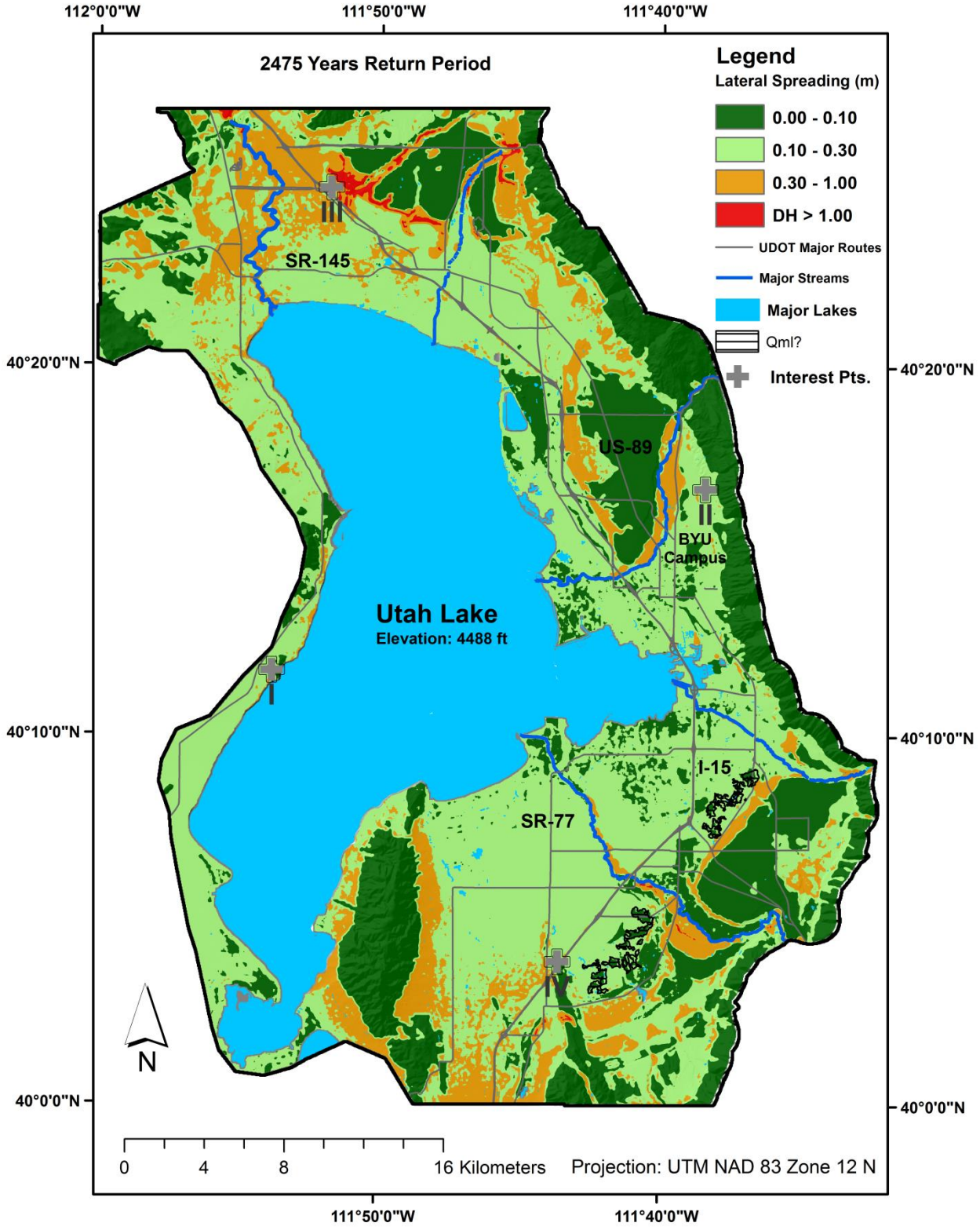

Fig. 5.7. The 2,475-year return period (2% probability of exceedance in 50 years) lateral spread hazard map, Utah County, Utah.

5.4 Discussion of the Lateral Spread Hazard Maps for Utah County

The lateral spread hazard maps shown in Figs. 5.6 and 5.7 highlight a major benefit of mapping the consequences of liquefaction rather than only liquefaction triggering. As shown in Chapter 4, the triggering hazard maps imply widespread liquefaction may occur during a major seismic event in Utah County; however, these maps do not indicate the severity of any ground failures induced by the liquefaction. Mapping the consequences, such as lateral spread displacements, provides a better estimate of potential damage to the built environment.

Although liquefaction may trigger, Fig. 5.6 shows that lateral spread displacements will generally not exceed 0.1 m for almost the entire study area at a return period of 1,033 years. The map does show some displacements may reach up to 0.3 m in some of the lacustrine sand and young alluvial fan units with sufficient topographic relief (i.e., near a free-face or on sloping ground). Generally speaking, a displacement less than 0.1 m will not cause damage, and a displacement of 0.1 to 0.3 m may only cause some minor damage. It is concluded that the lateral spread hazard is generally minimal at the 1,033-year return period.

For the much more extreme 2,475-year return period hazard, some locations in the study area may experience significant lateral spread displacements. Fig. 5.7 depicts portions of the study area that may undergo displacements greater than 1 m. Locales with the combined effect of sufficient values of $T_{15,cs}$, topographic relief, and apparent seismic loading may displace horizontally great distances during a more extreme earthquake. Even though the map does show significant lateral spread hazard at some locales, the majority of the map shows displacements that will not exceed 0.1 to 0.3 m. More research is needed to investigate why so much of the 2,475-year return period map has a frequent displacement hazard of 0.1 to 0.3 m. It is probable that this frequent hazard binning is partly due to the uncertainties in estimating $T_{15,cs}$ for an entire study

area. Further, when simulating a major earthquake (i.e., large apparent loading, L, value) as a result of the nearby Utah segment of the Wasatch Fault Zone, it appears to be so powerful that it frequently produces at least a small D_H value from 0.1 to 0.3 m in geologic units with nonzero $T_{15,cs}$ values.

Fig. 5.8 presents D_H-hazard curves at 4 points of interest, as located in Figs. 5.6 and 5.7. The figure highlights how the displacement hazard varies at some of the points in the study area. For example, Point III is near the I-15 corridor, north of Utah Lake. The lateral spread displacement hazard was greatest at this point as compared with the other points. Point I is west of Utah Lake and has the lowest displacement hazard as compared with the other points. This is likely because Point I has a lower apparent loading hazard as it is further from the Wasatch Fault Zone.

Lastly, as discussed in the previous chapter of this report, deposits labeled as "Qml?" in the geologic base map were hatched in the hazard maps in Figs. 5.6 and 5.7. Since none of the available geotechnical investigations were in these deposits, and since they may have underwent lateral spreading during a prehistoric earthquake, further research is needed to determine the lateral spread hazard for the *Qml?* deposits.

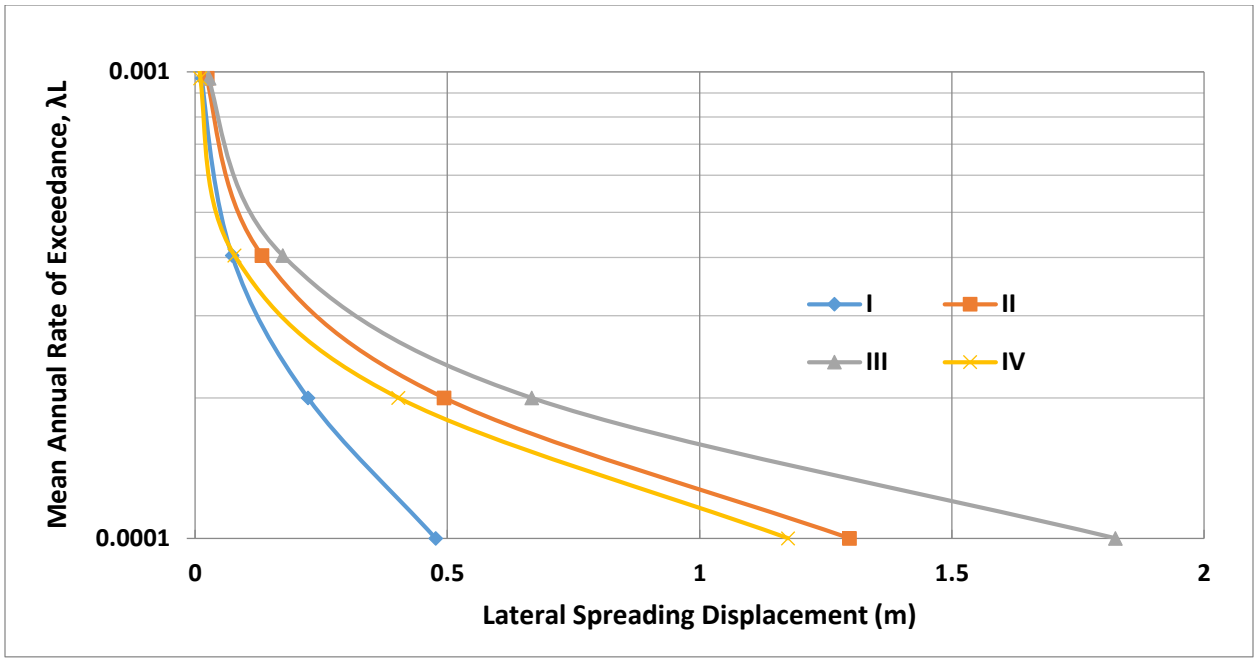

Fig. 5.8. Lateral spreading displacement hazard curves for 4 points of interest in the study area.

6. Conclusions

This paper proposed methods to map fully probabilistic liquefaction triggering and lateral spread displacement hazard maps using available seismic, geotechnical, geological and topographical data. The proposed methods were then implemented to produce liquefaction hazard maps at return periods of 475, 1033, and 2475 years for a regional area in Utah County, Utah. Although the report focused on Utah County, other areas in the United States could also be mapped following similar procedures.

The methods presented in this report are new and innovative. First, the liquefaction hazard maps are based on apparent seismic loading from a fully probabilistic seismic hazard analysis (PSHA). Previous liquefaction hazard mapping efforts (e.g., Anderson et al. 1994; Bartlett et al. 2005; Baise et al. 2006; Holzer et al. 2006; Olsen et al. 2007; Bartlett and Gillins 2013) show hazard levels given a constant peak ground acceleration for the entire study area, a scenario seismic event, or a single event from deaggregation of a probabilistic seismic hazard analysis. Modeling the entire PSHA is a new accomplishment for mapping liquefaction hazards. Second, using Monte Carlo random sampling techniques, the maps presented in this report modeled published errors in state-of-the-art liquefaction triggering (i.e., Idriss and Boulanger 2012) and lateral spread displacement (i.e., Gillins and Bartlett 2013) empirical equations. Lastly, the lateral spread hazard maps modeled the spatial variation in ground slopes and free faces using a highly-resolute digital elevation model developed from aerial lidar data collected just 3 years ago in 2013.

The maps are intended to convey hazard information to city planners, developers, and engineers. It is hoped that engineers can begin or continue performing site-specific analyses in areas mapped with high lateral spread hazard in order to refine the mapped estimates. Mapping liquefaction hazard for a regional area is challenging, and the authors recognize some parts of the

maps may have errors. Although the maps are based on hundreds of geotechnical investigations, significant uncertainties remain in the subsurface conditions and more investigations are necessary to reduce these errors. By conducting and compiling additional investigations, it would then be possible to update and improve the maps.

The authors strongly encourage people engaged in designing, building, or managing infrastructure—especially critical infrastructure—to hire an expert to perform site-specific liquefaction hazard analyses. Although the maps should be considered a step forward from previous hazard mapping efforts, the maps are still not intended nor recommended for site-specific engineering design. Local engineers should be consulted because they can provide expert knowledge of certain locations in the study area where they have previously conducted geotechnical investigations. Such engineers might also be able to note discrete areas on the maps that are over- or under-conservative based on their many years of experience testing and sampling the soil in Utah County. Nevertheless, it is highly recommended to still validate local opinions by performing site-specific testing as the authors noticed marked variability in the results of SPT investigations—even for SPT investigations in the same geologic unit within 100 m of each other. The authors attempted to account for this variability while mapping Utah County by developing distributions of geotechnical properties using tens to hundreds of available SPT investigations in each major geologic unit. It is inappropriate to assume that a few local SPT investigations at a discrete location adequately characterizes the uncertainties in subsurface conditions for an entire, widespread geologic unit in the study area.

The liquefaction triggering maps show widespread liquefaction hazard in the study area in Utah County. This is because: (1) numerous SPT borehole logs in the geotechnical database show layers of loosely deposited, cohesionless soils; (2) a significant portion of the area has a shallow

groundwater table due to its proximity to Utah Lake; and (3) the area is in very close proximity to the Utah segment of the Wasatch Fault Zone which is capable of generating a major earthquake with M = 7. Clearly, liquefaction should be a major concern for Utah County as well as other parts of the Wasatch Front. However, the triggering maps do not convey whether or not liquefaction will induce ground failures which may damage the built environment. For this reason, the lateral spread hazard maps are very useful for understanding the possible consequences of liquefaction. Lateral spreading is generally considered the most pervasive type of liquefaction-induced ground failure (NRC 1985), and it can be severely damaging to structures, bridges, retaining walls, pavements, and lifelines. The lateral spread hazard maps show a negligible displacement hazard at return periods of 475 years and 1033 years. However, at the more extreme 2475-year return period hazard, displacements may exceed 1 m in a few locations in the study area. It is recommended to conduct additional site-specific studies at areas with high lateral spread hazard. Further research is recommended to develop procedures to map other liquefaction-induced ground failures, such as vertical settlements and ground oscillations.

7. Acknowledgements

This research was supported by the U.S. Geological Survey (USGS), Department of the Interior, under USGS award numbers G14AP00118 and G14AP00119, as well as by the Utah Department of Transportation and the Central Utah Water Conservancy District. The views and conclusions contained in this document are those of the authors and should not be interpreted as necessarily representing the official policies, either expressed or implied, of these government agencies. We are grateful to these three agencies for their financial support and technical interest. We also would like to thank and acknowledge graduate students Mahyar Sharifi-Mood, Oregon State University, and Jasmyn Harper, Brigham Young University, for assisting with this research and contributing some of the text and figures in this report. Lastly, we would like to express appreciation to Dr. Steven Bartlett, associate professor at the University of Utah, for initiating and leading the Utah Liquefaction Advisory Group and for providing helpful recommendations and advice.

8. References

Anderson, L.R., Keaton, J.R., and Bischoff, J.E. (1994). "Liquefaction Potential Map for Utah County, Utah," Logan, Utah State University Department of Civil and Environmental Engineering and Dames and Moore unpublished Final Technical Report prepared for the U.S. Geological Survey, National Earthquake Hazards Reduction Program Award No. 14-08-0001-21359, 46 p., 1986; published as Utah Geological Survey Contract Report 94-8, 1994.

Anderson, L.R., Keaton, J.R., Aubrey, Kevin, and Ellis, S.J. (1982). "Liquefaction Potential Map for Davis County, Utah," Logan, Utah State University Department of Civil and Environmental Engineering and Dames and Moore unpublished Final Technical Report prepared for the U.S. Geological Survey, National Earthquake Hazards Reduction Program Award No. 14-08-0001-19127, 50 p.; published as Utah Geological Survey Contract Report 94-7, 1994.

Baise, L.G., Higgins, R.B., and Brankman, C.M. (2006). "Liquefaction Hazard Mapping – Statistical and Spatial Characterization of Susceptible Units." J. Geotech. & Geoenviron. Eng., Vol. 132, No. 6, 705-715.

Bardet, J.P., Tobita, T., Mace, N., and Hu, J., (2002). "Regional Modeling of Liquefaction-Induced Ground Deformation", Earthquake Spectra, 18(1), 19-46.

Bartlett S. F., Olsen, M. J., and Solomon, B. J., (2005). "Lateral Spread Hazard Mapping of Northern Salt Lake County for a Magnitude 7.0 Scenario Earthquake," Technical Report submitted to the United States Geological Survey, NERHP Award No. 04HQGR0026, 218 p.

Bartlett, S. F., and Youd, T. L. (1992). "Empirical Analysis of Horizontal Ground Displacement Generated by Liquefaction-Induced Lateral Spreads." *Technical Report NCEER-92-0021*, National Center for Earthquake Engineering Research, Buffalo, NY.

Bartlett, S.F., and Gillins, D.T., (2013). "Mapping the probability and uncertainty of liquefaction-induced ground failure for Weber County, Utah." USGS External Research Award No. G12AP20074, Earthquake Hazards Program, Denver, CO, 295 pp.

Bartlett, S.F., and Youd, T.L. (1995). "Empirical prediction of liquefaction-induced lateral spread." J. Geotech. Engrg., 121(4), 316-329.

Boulanger, R.W., and Idriss, I.M. (2005). "Evaluating cyclic failure in silts and clays," *Proc. of Geotechnical Earthquake Engrg. Satellite Conf. on Performance-Based Design in Earthquake Geotech. Engrg: Concepts and Research*. Prepared by TC4 Committee of ICSMGE, Japanese Geotechnical Society, Tokyo, 78-86.

Boulanger, R.W., and Idriss, I.M. (2012). "Probabilistic Standard Penetration Test-Based Liquefaction Triggering Procedure," J. Geotech. Geoenviron. Eng. 138(10), 1185-1195.

Boulanger, R.W., and Idriss, I.M. (2014). "CPT and SPT Based Liquefaction Triggering Procedures," *Report No. UCD/CGM-14/01, Center for Geotechnical Modeling*, Univ. of Calif. Davis, 138 pp.

Bray, J.D., and Sancio, R.B. (2006). "Assessment of the Liquefaction Susceptibility of Fine-Grained Soils," *Journal of Geotech. & Geoenvir. Engrg*., 132(9): 1165-1177.

Cetin, K. O., Seed, R. B., Kiureghian, A. D., Tokimatsu, K., Harder, L. F., Jr., Kayen, R. E., and Moss, R. E. (2004). "Standard Penetration Test-based probabilistic and deterministic assessment of seismic soil liquefaction potential." J. Geotech. Geoenviron. Eng. 130(12), 1314 – 1340.

Constenius, K.N., Clark, D.L., King, J.K., and Buck Ehler, J. (2011). "Interim Geologic Map of the Provo 30' x 60' Quadrangle, Utah, Wasatch, and Salt Lake Counties, Utah," *Open-File Report 586DM*, Utah Geological Survey.

EZ-FRISK 7.62 [Computer software]. Boulder, CO, Risk Engineering

Faris, A.T., Seed, R.B., Kayen, R.E., and Wu, J. (2006). "A semi-empirical model for the estimation of maximum horizontal displacement due to liquefaction-induced lateral spreading." Vol. 3, Proc., 8th U.S. Nat. Conf. Earthquake Engrg., Earthquake Engineering Research Institute, Oakland, CA, 1584-1583.

FEMA (2009). NEHRP Recommended Seismic Provisions for New Buildings and Other Structures, FEMA P-750/2009 Edition, Federal Emergency Management Agency, 406 pp.

Franke, K.W. (2005). "Development of a performance-based model for the prediction of lateral spreading displacements." M.S. thesis, Univ. of Washington, Seattle.

Franke, K.W. and Kramer, S.L. (2013). "Procedure for the Empirical Evaluation of Lateral Spread Displacment Hazard Curves." J. Geotech. & Geoenviron. Eng., 140(1), 2014.140:110-120.

Gillins, D.T. (2012). "Mapping the Probability and Uncertainty of Liquefaction-Induced Ground Failure," Ph.D. Dissertation, Univ. of Utah, Salt Lake City, 297 pp.

Gillins, D.T. (2014). "Considering Topography when Mapping Liquefaction Hazard with the Liquefaction Potential Index," *Proc. 10th National Conf. on Earthquake Engrg.*, Anchorage, Alaska, July 21-25, 12 pp.

Gillins, D.T. and Bartlett, S.F. (2013). "Multilinear Regression Equations for Predicting Lateral Spread Displacement from Soil Type and Cone Penetration Test Data." J. Geotech. & Geoenviron. Eng., 140(4), 04013047.

Hamada, M., Yasuda, S., Isoyama, R., and Emoto, K. (1986). "Study on liquefaction induced permanent ground displacements." *Report for the Association for the Development of Earthquake Prediction in Japan*, Tokyo, Japan, 87 pp.

Harty, K. and Lowe, M. (2003). UGS Special Study 104, "Geologic evaluation and hazard potential of liquefaction-induced landslides along the Wasatch Front, Utah".

Holzer, T.L., Blair, J.L., Noce, T.E., and Bennett, M.J. (2006). "LiqueMap: A Real-Time Post Earthquake Map of Liquefaction Probability." Proc., 8th US National Conference on Earthquake Eng., EERI, Oakland, CA.

Idriss, I.M., and Boulanger, R.W. (2004). "Semi-empirical procedures for evaluating liquefaction potential during earthquakes," Proc. of the 11th International Conf. on Soil Dynamics and Earthquake Engrg and 3rth International Conf. on Earthquake Geotechnical Engrg., Vol. I, 32-56.

Idriss, I.M., and Boulanger, R.W. (2008). *Soil liquefaction during earthquakes*, Earthquake Engineering Research Institute Monograph MNO-12, Earthquake Engineering Research Institute, Oakland, CA, 262 pp.

Idriss, I.M., and Boulanger, R.W. (2010). "SPT-Based Liquefaction Triggering Procedures," *Report No. UCD/CGM-10/02, Center for Geotechnical Modeling*, Univ. of Calif. Davis, 259 pp.

Kramer (1996). *Geotechnical Earthquake Engineering*, Prentice-Hall, Englewood Cliffs, New Jersey, 653 pp.

Kramer (2008). "Evaluation of Liquefaction Hazards in Washington State," *WSDOT Research Report No. WA-RD 668.1*, Washington State Department of Transportation, 329 pp.

Kramer, S.L. and Mayfield, R.T. (2007). "Return period of soil liquefaction." J. Geotech. & Geoenvir. Eng., ASCE. 133(7), 802-813.

Kulhawy, F.H., and Mayne, P.W. (1990). *Manual on Estimating Soil Properties for Foundation Design*, Report EPRI EL-6800, Electric Power Research Institute, Palo Alto, CA.

Moss, R. E. S., Seed, R. B., Kayen, R. E., Stewart, J. P., Kiureghian, A. D., and Cetin, K. O., 2006. CPT-based probabilistic and deterministic assessment of in situ seismic soil liquefaction potential, *J. Geotech. Geoenviron. Eng.* **132**(8), 1032 – 1051.

National Research Council (NRC) (1985). Liquefaction of Soils During Earthquakes, National Academy Press, Washington D.C., 240 p.

Olsen, M. J., Bartlett, S. F., and Solomon, B. J., (2007). "Lateral Spread Hazard Mapping of the Northern Salt Lake Valley, Utah, for M7.0 Scenario Earthquake," Earthquake Spectra, 23(1), 95-113.

Petersen, M. D., Frankel, A. D., Harmsen, S. C., Mueller, C. S., Haller, K. M., Wheeler, R. L., Wesson, R. L., Zeng, Y., Boyd, O. S., Perkins, D. M., Luco, N., Field, E. H., Wills, C. J., and Rukstales, K. S., 2008. *Documentation for the 2008 Update of the United States National Seismic Hazard Maps, U.S. Geological Survey Open-File Report 2008–1128*, Reston, VA, 61 pp.

Rauch, A.F., and Martin, J.R. (2000). "EPOLLS Model for Predicting Average Displacements on Lateral Spreads", J. Geotech. & Geoenvir. Eng., ASCE, 126(4), 360-371.

Seed, H.B. (1979). "Soil liquefaction and cyclic mobility evaluation for level ground during earthquakes," *Journal of Geotechnical Engineering Div.* **105**(2), 201-255.

Seed, H.B., and Idriss, I. M. (1971). "Simplified Procedure for Evaluating Soil Liquefaction Potential," *Journal of Soil Mechanics and Found. Div.* **97**(9), 1249-1273.

Seed, H.B., and Idriss, I.M., (1982). "Ground Motions and Soil Liquefaction During Earthquakes," Earthquake Engineering Research Institute Monograph.

Seed, H.B., Tokimatsu, K., Harder, L.F., and Chung, R.M. (1985). "Influence of SPT Procedures in Soil Liquefaction Resistance Evaluations," *Journal of Geotech. Engrg. Division*, ASCE, 111(12).

Stewart, J.P., Liu, A.H., and Choi, Y. (2003). "Amplification Factors for Spectral Acceleration in Tectonically Active Regions," *Bulletin of the Seismological Society of America*, 93(1), 332-352.

Youd, T. L., Idriss, I. M., Andrus, R. D., Arango, I., Castro, G., Christian, J. T., Dobry, R., Finn, W. D. L., Harder, L. F., Jr., Hynes, M. E., Ishihara, K., Koester, J. P., Liao, S. S. C., Marcuson, W. F., III, Martin, G. R., Mitchell, J. K., Moriwaki, Y., Power, M. S., Robertson, P. K., Seed, R. B., Stokoe, K. H., II (2001). Liquefaction resistance of soils: summary report from the 1996 NCEER and 1998 NCEER/NSF workshops on evaluation of liquefaction resistance of soils, *J. Geotech. Geoenviron. Eng*. **127**(10), 817-833.

Youd, T. L., Hansen, C. M., and Bartlett S. F. (2002). Revised multilinear regression equations for prediction of lateral spread displacement." J. Geotech. Geoenviron. Eng. 128(12), 1007-1017.

Youd, T.L., and Perkins, D.M. (1978). Mapping liquefaction-induced ground failure potential, *Journal of the Geotechnical Engineering Division* **104**, No. GT4, 433-446.

Youd, T.L., and Perkins, D.M. (1987). "Mapping of liquefaction severity index." J. Geotech. Eng. 113(11), 1374-1392.

Zhang, G., Robertson, P. K., and Brachman, R. W. (2004). "Estimating liquefaction-induced lateral displacements using the standard penetration test or cone penetration test." J. Geotech. Geoenviron. Eng. 130(8), 861-871.

9. Appendix

Table A 1: Description of Data Fields for Site Table

Field Name	Description	Units
BOREELEV	Surface elevation of SPT borehole	feet
BORING	Identification of borehole listed on SPT log	[text]
BoreDiam	Diameter of borehole	inches
BoreDiamEs	Quality indicator of diameter of borehole: 1 = directly from log; 2 = from log drilled by same rig and driller	
DATE_	Date of borehole	[text]
DEPTHGW	Depth to groundwater table	feet
DRILLER	Name of company who drilled the borehole	[text]
DRILLMETH	Drilling method	[text]
ELEVEST	Quality indicator for elevation of borehole: 1 = directly from log; 2 = estimated from nearby log; 3 = from maps	
GWDATE	Date of depth to groundwater measurement	[text]
GWEST	Quality indicator of depth to groundwater measurement; 1 = directly from log at least 24 hours after drilling; 2 = from log but date not listed; 3 = from nearby log	
HAMMER_TYP	Hammer type (i.e., safety, donut, or automatic)	[text]
LATITUDE	NAD 1983 latitude (in decimal degrees)	degree
LATITEST	Quality indicator of measurements of latitude and longitude: 1 = directly from log; 2 = scaled from maps	
LONGITUDE	NAD 1983 longitude (in decimal degrees)	degree
NCORR	True/False whether SPT N-values on logs were already corrected to $N_{1,60}$	
NOTES	Notes and other information	[text]
REFERENCE	Name of folder containing scanned images of SPT logs	
REPORT	Name of report where SPT log can be found	[text]
RIGTYPE	Type of drill rig used by drillers	[text]
SITEIDNO	Identification number assigned to SPT (link to BLOW table)	
SITENAME	Name of facility or address where SPT was performed	[text]
EASTING	NAD 1983, UTM Zone 12 easting	meters
NORTHING	NAD 1983, UTM Zone 12 northing	meters
CE	Mean correction for hammer energy ratio : 1 = safety; 1.1 = automatic. Apply to correct raw SPT blow counts to $N_{1,60}$	
CB	Correction for borehole diameter. Apply to correct raw SPT blow counts to $N_{1,60}$	
GEOLUNIT	Mapped surficial geologic unit where SPT was performed	[text]

Table A 2: Description of data fields for BLOW table

Field Name	Description	Units
BOREIDNO	Identification of boring listed on SPT log	[text]
COMMENTS	Comments or additional information	[text]
DEPTH	Depth to middle of sample or depth to boundary line between layers	feet
DRYUNIT	Dry unit weight of sample	kN/m^3
DRYUNITPCF	Dry unit weight of sample in pounds per cubic foot	pcf
ESTATT*	Quality indicator for Atterberg limits of sample	
ESTDRY*	Quality indicator for dry unit weight of sample	
ESTFINES*	Quality indicator for fines content of sample	
ESTMOIST*	Quality indicator for moisture content of sample	
ESTNM*	Quality indicator for SPT blow counts for bottom 12 inches (0.3 m) of sample	
ESTUSCS*	Quality indicator for classification of sample according to the Unified Soil Classification System	
ESTWET*	Quality indicator for wet unit weight of sample	
FINES	Fines content of sample (percent of sample passing a U.S. Standard No. 200 sieve)	%
LIQUIDLIMIT	Liquid limit of sample	%
MOISTURE_ CONTENT	Moisture content of sample	%
N160	Corrected SPT blow counts ($N_{1,60}$) from borehole log for bottom 12 in. (0.3 m) of sample	
NVALUE	Uncorrected SPT blow counts for bottom 12 in. (0.3 m) of sample (more common than N160)	
PERGRAVEL	Percent of sample retained on a No. 4 sieve	%
PERSAND	Percent of sample passing a No. 4 sieve and retained on a No. 200 sieve	%
PLASTICINDEX	Plastic index of sample	%
PLASTICLIMIT	Plastic limit of sample	%
SAMPLER	Type of sampler: CS or MCAL = modified California; DM = Dames & Moore; SH = thin-walled Shelby tube; SS = split-spoon (standard for SPT)	
SAMPLEREST	Quality indicator for properties of sampler	
SAMPLER-LENGTH	Length sample retained in the sampler	feet
SAMPLER_ OUTSIDE_ DIAMETER	Outside diameter of sampler	inches
SITEIDNO	Identification number assigned to SPT (link to SITE table)	
SOILTYPE	Description of soil sample from log; blank values indicate boundary lines between layers	[text]
SPGRAV	Specific gravity of sample	
USCS	Unified Soil Classification System	[text]
WETUNIT	Wet unit weight of sample	pcf
WCLASS	Index assigned to sample for estimating its unit weight	
MCLASS	Index assigned to sample for estimating its moisture class	
SGCLASS	Index assigned to sample for estimating its specific gravity	
N60CE	SPT blow counts for bottom 12 in. (0.3 m) of sample, corrected for rod length, sampler liner, sampler type, and borehole diameter (but not for energy ratio, C_E)	
SOIL_INDEX	Soil index of sample (*SI*)	

* = A value of: 1 = directly from log; 2 = from nearby log in same report; 3 = from nearby log of different report; 9 = from log but likely inaccurate

Table A 3: Description of data fields for SITECPT table

Field Name	Description	Units
CONEID	Identification number of cone used for test	[text]
CPTIDNO	Identification number assigned to CPT	
DATE_	Date of sounding	[text]
DEPTHGW	Depth to groundwater table	feet
ELEV	Surface elevation of CPT sounding	feet
ELEVEST	Quality indicator for elevation of sounding: 3 = from map	
GWEST	Quality indicator of depth to groundwater measurement; 1 = from pore-water dissipation (PPD) test; 2 = from nearby PPD test ; 3 = interpolated between PPD tests	
LATITUDE	NAD 1983 latitude (in decimal degrees)	degree
LATITEST	Quality indicator of measurements of latitude and longitude: 1 = directly from log; 2 = scaled from maps; 3 = scale from maps of lesser quality	
LONGITUDE	NAD 1983 longitude (in decimal degrees)	degree
PROJECT	Name of folder containing raw CPT data	
REPORT	Name of report where CPT log can be found	[text]
SOUNDING	Identification of CPT sounding from logs	[text]
SOURCE	Name of company who performed the CPT	[text]
AREA_RATIO	Net area ratio of the cone	
EASTING	NAD 1983, UTM Zone 12 easting	meters
NORTHING	NAD 1983, UTM Zone 12 northing	meters
INCREMENT	Change in depth between CPT measurements	meters
GEOLUNIT	Mapped surficial geologic unit where CPT was performed	[text]

Table A 4: Description of data fields for CPTDATA table

Field Name	Description	Units
CPTIDNO	Identification number assigned to CPT (link to SITECPT table)	
DEPTH	Depth below ground surface	feet
PRESSURE	Pore-water pressure behind tip of cone (in feet of head)	feet
QC	Cone tip resistance	tsf
QT	Cone tip resistance corrected for pore-pressure effects	tsf
SLEEVE	Sleeve friction	tsf
SOUNDING	Identification of CPT sounding from logs	[text]
UBT	Pore-water pressure behind tip of cone (in tsf)	tsf
FRATIO	Friction ratio (SLEEVE/QT*100)	%
DEPTHM	Depth below ground surface, in meters	meters